nature catalysis

Article

https://doi.org/10.1038/s41929-023-01048-6

Sub-micro- and nano-sized polyethylene terephthalate deconstruction with engineered protein nanopores

Received: 7 March 2022

Accepted: 19 September 2023

Published online: 19 October 2023

Check for updates

Ana Robles-Martín[1,2,6], Rafael Amigot-Sánchez[3,6], Laura Fernandez-Lopez[4,6], Jose L. Gonzalez-Alfonso[4], Sergi Roda[1], Víctor Alcolea-Rodriguez[4], Diego Heras-Márquez[3], David Almendral[4], Cristina Coscolín[4], Francisco J. Plou[4], Raquel Portela[4], Miguel A. Bañares[4], Álvaro Martínez-del-Pozo[3], Sara García-Linares[3] ✉, Manuel Ferrer[4] ✉ & Víctor Guallar[1,5] ✉

The identification or design of biocatalysts to mitigate the accumulation of plastics, including sub-micro- and nano-sized polyethylene terephthalate (nPET), is becoming a global challenge. Here we computationally incorporated two hydrolytic active sites with geometries similar to that of *Idionella sakaiensis* PET hydrolase, to fragaceatoxin C (FraC), a membrane pore-forming protein. $FraC_{m1/m2}$ could be assembled into octameric nanopores (7.0 nm high × 1.6–6.0 nm entry), which deconstructed (40 °C, pH 7.0) nPET from GoodFellow, commodities and plastic bottles. $FraC_{m1}$ and $FraC_{m2}$ degrade nPET by endo- and exo-type chain scission. While $FraC_{m1}$ produces bis(2-hydroxyethyl) terephthalate as the main product, $FraC_{m2}$ yields a high diversity of oligomers and terephthalic acid. Mechanistic and biochemical differences with benchmark PET hydrolases, along with pore and nPET dynamics, suggest that these pore-forming protein catalytic nanoreactors do not deconstruct macro-PET but are promising in nanotechnology for filtering, capturing and breaking down nPET, for example, in wastewater treatment plants.

The World Economic Forum forecasted that by 2050 the production and use of plastics will grow at a rate of 4% per year[1,2], making them the most common waste material in the world, accounting for >380 million tons. Their cumulative greenhouse gas emissions from production to disposal may be equivalent to 10–13% of the total carbon budget; 10.2% are predicted to correspond to polyethylene terephthalate (PET) plastics[3,4]. Approximately 80% of waste objects are composed of macroplastics, with PET accounting for 14.4% of total plastic waste[1–4], which can reach the oceans from land[2,5], and be degraded over time to microplastics (5 mm to 1 µm), sub-microplastics (100 nm to 1 µm), and nanoplastics (1 nm to 100 nm)[1,2,6]. Recent studies confirmed that PET particles comprise at least 5% of the total identified plastic particles[1,2], which can be found in concentrations equivalent to trillions of particles in the air of some cities[7], from 2,649 to 6,292 particles per litre in mineral water[8], and from 5 to 52.3 ng ml^{-1} in mountain and Antarctica ice samples[9]. The ubiquity of plastic debris is causing an unprecedented ecological crisis[1,2].

[1]Barcelona Supercomputing Center, Barcelona, Spain. [2]Universitat de Barcelona, Barcelona, Spain. [3]Departamento de Bioquímica y Biología Molecular, Facultades de Medicina, Biología y Ciencias Químicas, Universidad Complutense, Madrid, Spain. [4]Instituto de Catalisis y Petroleoquimica, Consejo Superior de Investigaciones Científicas, Madrid, Spain. [5]Institució Catalana de Recerca i Estudis Avançats, Barcelona, Spain. [6]These authors contributed equally: Ana Robles-Martín, Rafael Amigot-Sánchez, Laura Fernandez-Lopez. ✉e-mail: sglinares@ucm.es; mferrer@icp.csic.es; victor.guallar@bsc.es

https://doi.org/10.1038/s41929-023-01048-6

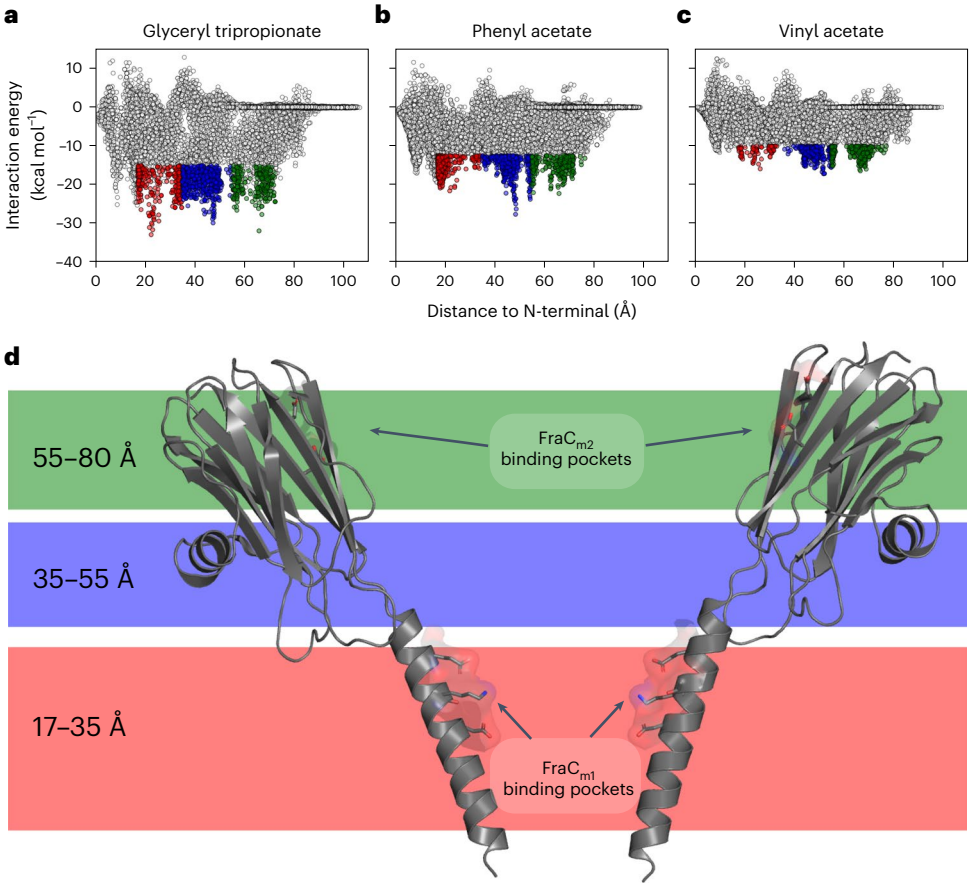

Fig. 1 | Global exploration of FraC binding site pockets using PELE. a, Energy profile of the global exploration with the branched ester glyceryl tripropionate and poses highlighted with the colour from each binding site (poses are highlighted only when the interaction energy is equal to or below −15 kcal mol^{-1}). **b**, Energy profile of the global exploration with the aromatic small-sized phenyl acetate and poses highlighted with the colour from each binding site (poses are only highlighted when the interaction energy is equal to or below −12.5 kcal mol^{-1}). **c**, Energy profile of the global exploration with the short chain alkenyl ester vinyl acetate and poses highlighted with the colour from each binding site (poses are highlighted only when the interaction energy is equal to or below −10 kcal mol^{-1}). **d**, Cross-sectional representation of FraC with two opposing chains to visualize the localization of the different indicated binding sites (Protein Data Bank (PDB) ID: 4TSY). Computational data were collected and analysed with PELE. Calculations and raw data are shown in Supplementary Data 1.

PET recycling is theoretically attainable[10,11], compared with other extremely challenging plastics, such as thermosets[6]. While there are more widely used and better established chemical recycling methods for PET[10], enzymatic PET recycling and upcycling strategies have been demonstrated as necessary alternatives[10,11]. Over the past 18 years, only a few benchmark enzymes from cultured and uncultured microorganisms have been shown to degrade macro-PET[12], some of which have been engineered to increase the stability (up to +37.5 °C) and activity at temperatures close to or exceeding the PET glass transition temperature (T_g), ~70 °C. This temperature is recommended to access amorphous regions of PET polymer[12], as it is physically impossible to enzymatically degrade crystalline PET, having a melting temperature (T_m) of 260 °C (Supplementary Note 1). Notable engineered examples are ThermoPETase[13] and HotPETase[14] from *Idionella sakaiensis*, and LCC_{ICCG} and LCC_{WCCG} from leaf-branch compost[15]. Although challenging[12], the degradation of PET below T_g has also been reported, notably, for the machine learning-engineered variant FAST-PETase that completely depolymerizes at 50 °C untreated postconsumer-PET[16], and for the *I. sakaiensis* PETase (*Is*PETase), active at 30 °C but labile at 37 °C after 24 h of incubation[12,17], and its redesigned variant DuraPETase that is long-term active at 37 °C (ref. 18).

Micro-, sub-micro- and nano-PET, hereinafter referred to as nPET, pollution has also been targeted for enzymatic deconstruction. DuraPETase degrades PET microplastics (10–50 µm) and nanoplastics (50–100 nm) at concentrations (0.2–0.3 g l^{-1}) 100-fold higher than those in wastewater plants, within 20 days at 37 °C (micro-) and within 1 h at 37 °C (nano-)[18]. The PETase from *Thermobifida fusca*, *Tf*Cut2, degrades nPET (100–164 nm) at 60 °C (refs. 19,20). These studies demonstrated the potential of PETases to also ameliorate nPET pollution, a line that we want to explore in this study, by designing a protein capable of filtering and degrading nPET. Within this context, actinoporins constitute a group of small and basic α pore-forming toxins produced by sea anemones as a defence mechanism[21]. In water, these easily produced and purified non-catalytic proteins remain perfectly soluble and stably folded; however, upon interaction with lipid membranes of a specific composition, they spontaneously become oligomeric integral membrane structures and make a pore[22]. Because of their physicochemical properties and configuration, most efforts towards designing pore-forming toxins have been directed at sensing molecules and sequencing[23,24].

In this Article, we generated a pore-forming catalytic enzyme that could be further assembled into catalytic nanopores/nanoreactors that act as a reaction chamber to degrade nPET. This advance can be addressed due to recent modelling developments in designing de novo active sites[25,26]. As a target, we selected fragaceatoxin C (FraC) from *Actinia fragacea*, the only actinoporin membrane pore with a three-dimensional structure solved with atomic resolution[21]. FraC is a stable 7-nm-high octameric V-shaped pore formed by spontaneous

https://doi.org/10.1038/s41929-023-01048-6

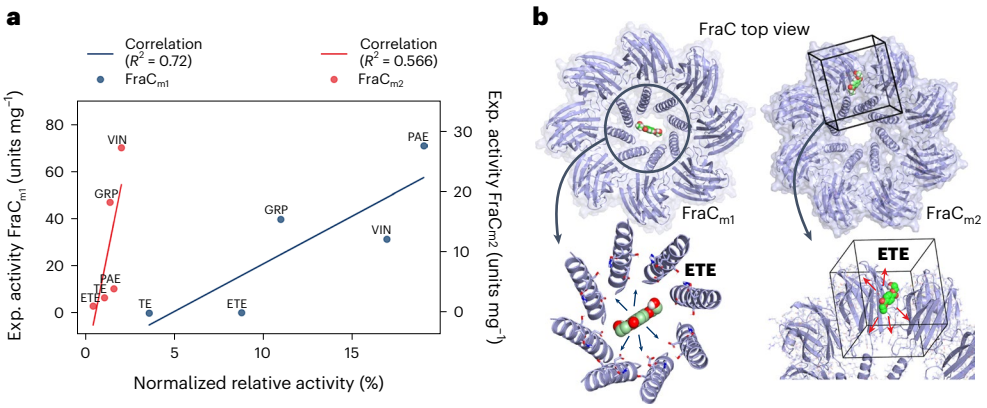

Fig. 2 | PELE Local Exploration of the different substrates in FraC$_{m1}$ and FraC$_{m2}$. a, Correlation between computational PELE normalized relative activity (number of catalytic PELE poses/total number of accepted PELE steps and number of ester groups in the substrate) and experimental ester-hydrolysing activity ('Exp. activity' in the figure) for glyceryl tripropionate (labelled as GRP), vinyl acetate (VIN), phenyl acetate (PAE), **TE** and **ETE**. **b**, Schematic representation of PELE Local Exploration with **ETE**. Arrows indicate the random movement of the substrate in an N-terminal Å box during the PELE local sampling simulation. Calculations and raw data provided in Supplementary Data 1.

self-assembly of the protein monomers and with access sizes on the order of 6.7 nm in the *cis* entry and on the order of 1.9 nm in the *trans* exit. A computational structure-based modelling method, the *PluriZyme* strategy[26,27], was applied to add an artificial catalytic serine–histidine–aspartic triad and an oxyanion hole capable of ester hydrolysis to the non-catalytic FraC. These catalytic elements match the active sites of PETases[12]. When two newly engineered catalytic proteins (FraC$_{m1}$ and FraC$_{m2}$) were assembled as nanopores (npFraC$_{m1}$ and npFraC$_{m2}$) they became pore-based nanoreactors for the depolymerization of nPET. We discovered different degradation product profiles between them and in comparison with benchmark PETases, namely LCC$_{WT}$, LCC$_{WCCG}$ and *Is*PETase[12,15].

Results

In silico design of catalytic pore-forming proteins

The entire inner surface of the wild-type FraC pore structure, FraC$_{WT}$, was explored using Protein Energy Landscape Exploration (PELE) software[26,27], using as probes three esters (Supplementary Fig. 1) commonly hydrolysed by most esterases and lipases[26]. As in PluriZyme designs[26,27], the initial goal is applying PELE to identify substrate binding sites for designing artificial hydrolase active sites. Energetic profiles of FraC$_{WT}$ from these simulations (Supplementary Data 1) are shown in Fig. 1a–c, in which the binding energy minima are split into three regions based on the distance to the *trans* exit of the pore. Notably, the three substrates found good pockets at similar distances, denoting a suitable ester stabilizing environment. As shown in Fig. 1d, from the *cis* side to the *trans* side, the outer cluster corresponds to the globular domain of the monomer at 70 Å from the bottom side (a more solvent-exposed side). The second cluster, located at a distance between 35 Å and 55 Å, corresponds to the hinge region of the monomer and is characterized by the presence of highly conserved residues involved in the conformational change forming the nanopore. We discovered several minima in this region but rejected them to avoid a loss of pore-forming activity[28]. At a distance of 20 Å, we discovered the transmembrane region configured by the N-terminal α-helices, where pockets are formed by non-conserved polar side chains facing the inner part of the channel. Both the first cluster and third cluster fulfilled our goal of introducing hydrolytic sites into the main pore, the dimensions/shapes of which can assist in channelling and holding substrates once they are assembled.

Interestingly, two acidic residues, Asp17 and Glu24, lie in the vicinity of the identified transmembrane pocket. In general, the insertion of a negative charge into a structure is detrimental, so we typically take advantage of the presence (if any) of acidic residues. Following this approach, the Lys20His and Thr21Ser variant introduced intra- and interhelix catalytic triad hydrogen bonds. Regarding the outer pocket, we also identified several acidic residues, Asp38, Glu40 and Glu173. In this case, there is also a native histidine, His175; PELE simulations revealed that the Asp38Ser variant could generate a catalytic triad. Moreover, we wanted to add a mutation that could act as an oxyanion hole to stabilize the negative charge that appears during hydrolysis: Glu173Gln.

The potential catalytic poses involving an ester carbon-serine oxygen distance <4.5 Å concurrent with hydrogen bonds between Ser–His and His–Asp/Glu were quantified for the three exploration model esters and the two variants, FraC$_{m1}$, including Lys20His and Thr21Ser, and FraC$_{m2}$, including Asp38Ser and Glu173Gln. The computed PELE-normalized relative catalytic activity ranged from 19.01% to 10.98% for FraC$_{m1}$ and from 2.05% to 1.42% for FraC$_{m2}$ (Fig. 2a and Supplementary Data 1). Furthermore, the computed PELE-normalized relative catalytic activity for bis(2-hydroxyethyl)-terephthalate (or **ETE**, following the nomenclature by Schubert et al.[29]), and mono-(2-hydroxyethyl)-terephthalic acid (or **TE**), which are incomplete degradation products during the hydrolysis of PET by PETases[12] (Extended Data Fig. 1), ranged from 8.79% to 3.61% for FraC$_{m1}$ and from 0.47% to 1.10% for FraC$_{m2}$ (Fig. 2a). FraC$_{m1/m2}$ active sites can thus potentially accommodate and convert ester substrates, including **TE** and/or **ETE**. Note that although both our designs (FraC$_{m1/m2}$) and *Is*PETase[30] share an analogous active site geometry (Supplementary Fig. 2), as seen by clarifying the enzyme–substrate encounter complex by quantum/molecular mechanics (QM/MM) (Supplementary Data 1), the overall FraC$_{m1/m2}$ pore is formed by eight different chains (Fig. 2b)[21], thus introducing eight potential catalytic triads after pore assembly compared with the monomeric *Is*PETase[30].

The stability of both the soluble form and the N-terminal region inserted into a membrane model by molecular dynamics (MD) was further confirmed (Supplementary Figs. 3–6). The analysis of catalytic distances for the inserted models indicated adequate hydrogen bond values, with the histidine–serine distance along the simulation being lower for the N-terminal mutant FraC$_{m1}$ (Fig. 3a–d) than for the globular mutant FraC$_{m2}$ (Fig. 3e–h).

We further evaluated whether the two active centres, located inside the nanopores, could be accessed by nPET particles. Although the flexible nature of a single chain cannot directly be translated to that of a PET particle, we explored the flexibility of a PET chain of 200 units (which could mimic the molecular weights of various common PET samples, from 40 to 80 kDa) with MD simulations. The simulation

https://doi.org/10.1038/s41929-023-01048-6

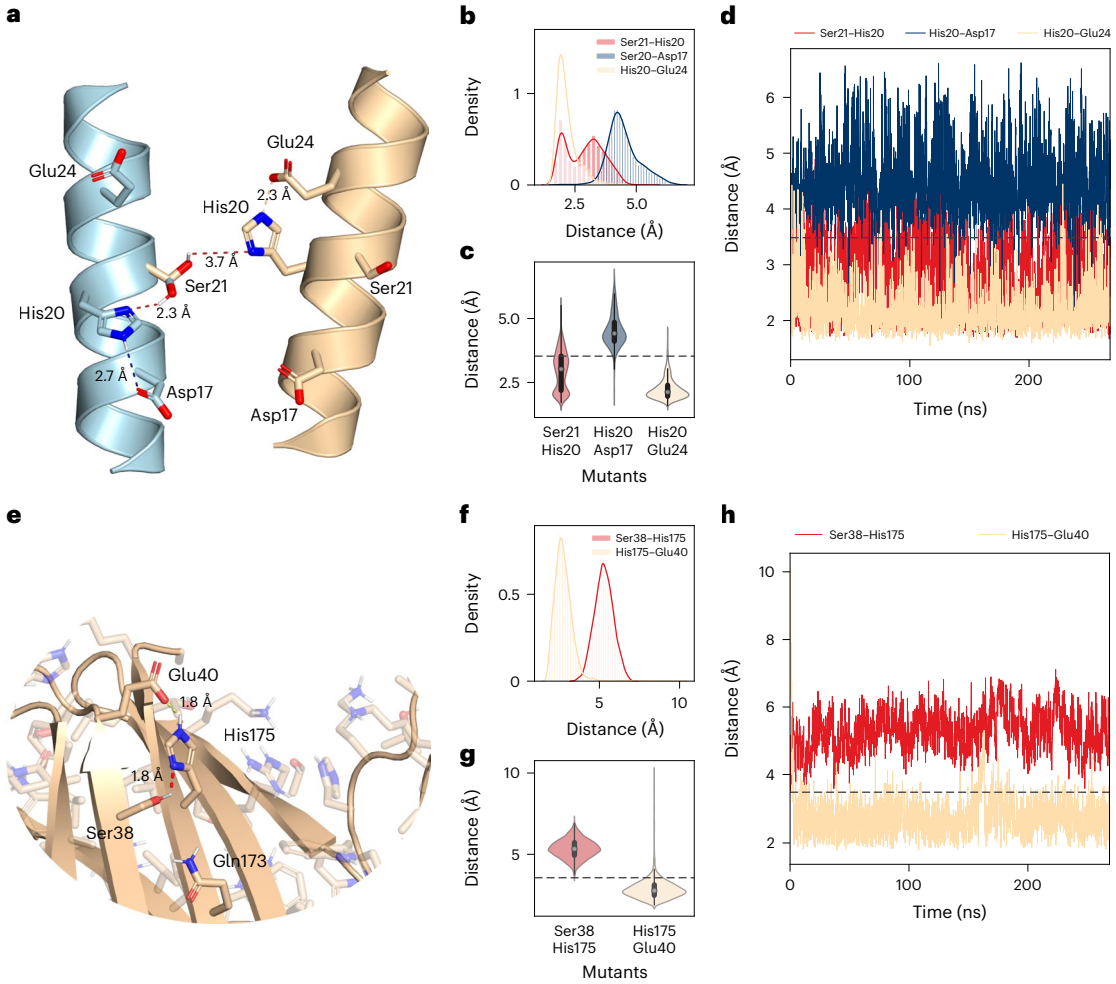

Fig. 3 | Membrane MD simulation of FraC$_{m1}$ and FraC$_{m2}$. FraC$_{m1}$: **a**, N-terminal fragments are shown from residues 13 to 28, where the catalytic active site is located. Ser21 (introduced by a Thr21Ser mutation), His20 (introduced by a Lys20His mutation) and Glu24 (detected in the wild-type protein) formed the catalytic triad, and Asp17 and Glu24 (both detected in the wild-type protein) could act as the acid residue of the catalytic triad due to the proximity of the histidine residue. Hydrogen bond interactions between catalytic residues and their distances are displayed. **b**,**c**, Histogram (**b**) and violin plot (**c**) of the distances between two catalytic residues in the catalytic triad throughout the simulation. **d**, Distance between two catalytic residues over the simulation time. FraC$_{m2}$: **e**, The active site in the globular region is shown. Ser38 (introduced by an Asp38Ser mutation), His175 (detected in the wild-type protein) and Glu40 (detected in the wild-type protein) conformed to the catalytic triad, and Gln173 (introduced by a Glu173Gln mutation) in the vicinity of the identified pocket conformed to the oxyanion hole. **f**,**g**, Histogram (**f**) and violin plot (**g**) of the distances between two catalytic residues in the catalytic triad throughout the simulation. **h**, Distance between two catalytic residues over the simulation time. MD simulations were collected and analysed with GROMACS (version 5.1.2) and OPENMM (version 7.3). Calculations and raw data are provided in Supplementary Data 1.

shows that the PET chains in the nPET particle are dynamic entities and that their shape changes considerably over time (Fig. 4a), introducing multiple protuberances that could fit the pore dimensions, as observed in simple molecular docking (Fig. 4b). Moreover, one would expect that these protuberances could be stabilized by the pore shape (in an induced fit manner) and increase with partial hydrolysis. Moreover, one could also anticipate these particles to be formed from various chains, having multiple loose ends.

npFraC$_{m1}$ and npFraC$_{m2}$ catalyse ester hydrolysis of TE and/or ETE

FraC$_{WT}$, FraC$_{m1}$ and FraC$_{m2}$ were produced in an *Escherichia coli* expression system and purified (at least 95% pure; Supplementary Fig. 7 and Source Data). After evaluating that the intrinsic features and activities of the two mutants were indistinguishable from those of the wild type (Supplementary Fig. 8a–d and Supplementary Data 2), they were assembled as individual octameric pore water-soluble particles by adding them to empty nanodiscs to mimic the real situation encountered by actinoporins[21] (Supplementary Fig. 9 and Source Data). See details in Supplementary Note 2. These preparations, referred to as npFraC$_{WT}$, npFraC$_{m1}$ and npFraC$_{m2}$, were tested for their hydrolytic activity (Supplementary Note 3).

The measurement of *p*-nitrophenol (*p*-NP) release showed that npFraC$_{m1}$ and npFraC$_{m2}$ were capable of hydrolysing the three *p*-NP esters tested (pH 7.0, 40 °C), which are model esters for serine ester hydrolases (Extended Data Table 1 and Supplementary Data 3). Both engineered nanopores hydrolysed (pH 7.0, 40 °C) also the three model esters used for PELE exploration, **ETE** and **TE**, although npFraC$_{m1}$ showed low specific activity for **TE** (Extended Data Table 1 and Supplementary Data 3). We observed notable correlations between the computed PELE-normalized relative catalytic activity and the experimental ester-hydrolysing activity ($R^2 = 0.72$ for npFraC$_{m1}$; $R^2 = 0.566$ for npFraC$_{m2}$; Fig. 2a). npFraC$_{m1}$ and npFraC$_{m2}$ hydrolysed **ETE** with k_{cat}/K_m values (Table 1, Supplementary Fig. 10 and Supplementary Data 4) that were directly benchmarked with those reported for PETases (550–17,000 $M^{-1}\,s^{-1}$)[31].

https://doi.org/10.1038/s41929-023-01048-6

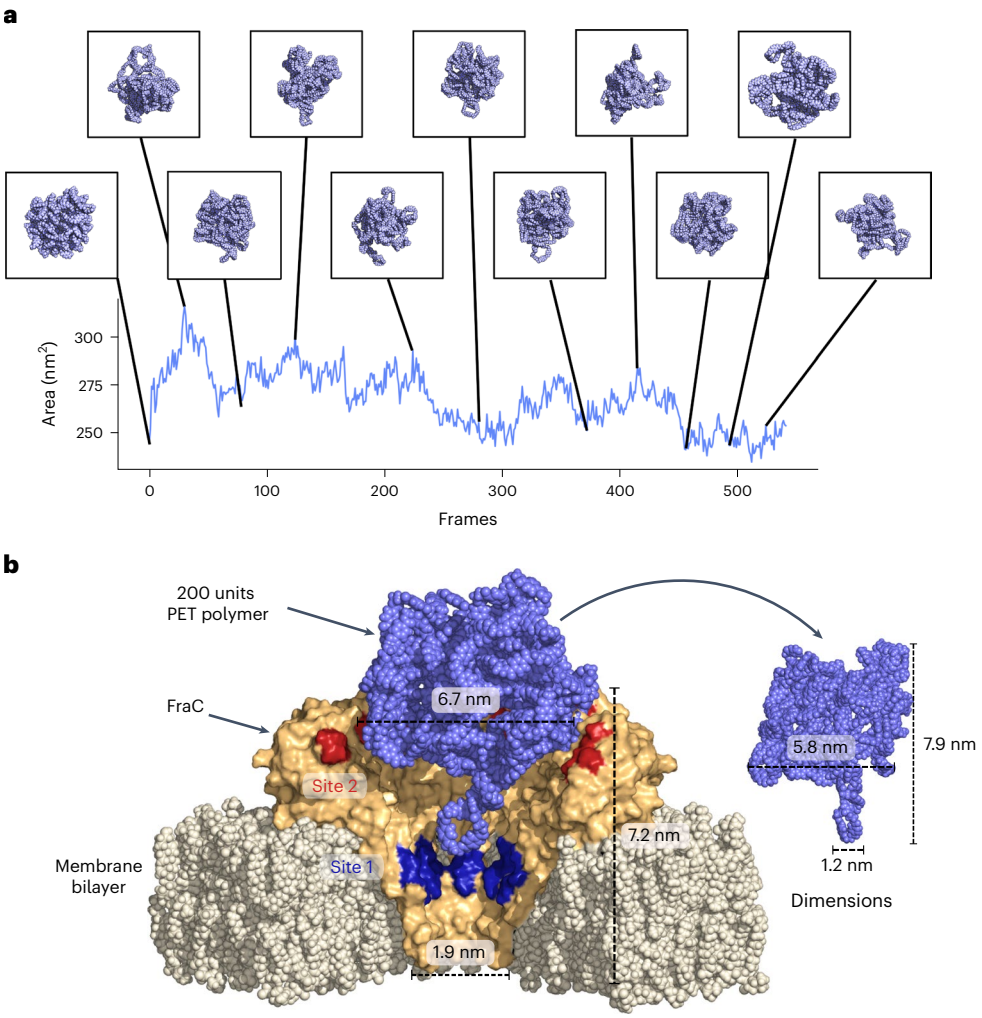

Fig. 4 | Molecular dynamic simulation of PET in solution. a, Solvent-accessible surface area of a nPET particle of 200 monomers over ~50 ns and 40 °C. Snapshots from the simulation are shown for different frames (where a frame is 0.1 ns). **b**, Graphical representation of a schematic coupling between the pore and the polymer. Calculations and raw data are provided in Supplementary Data 1.

Using *p*-NP propionate as a substrate under different conditions, npFraC$_{m1}$ and npFraC$_{m2}$ showed maximum hydrolytic activity at a pH of approximately 9.0 and temperatures from 35 °C to 45 °C (Supplementary Fig. 11 and Supplementary Data 5). This is strongly consistent with the experimentally determined thermal melting temperature of FraC$_{WT}$ (T_m = 55.3 ± 0.5 °C), FraC$_{m1}$ (T_m = 57.4 ± 0.5 °C) and FraC$_{m2}$ (T_m = 61.6 ± 0.5 °C), as monitored by circular dichroism spectroscopy at 220 nm (Supplementary Fig. 12 and Supplementary Data 6).

Deconstruction of nPET by npFraC$_{m1/m2}$

We further evaluated the possibility that npFraC$_{m1}$ and npFraC$_{m2}$ not only hydrolyse **TE** and **ETE** but also break down nPET particles of different types across the pores. Instead of using naturally occurring nPET particles, for example, those in wastewater treatment plants[18], we chose to prepare, in vitro, particles of different nature. This allows us to assess their physical–chemical characteristics and their alterations during the degradation process, and the released products. nPET particles were produced (Supplementary Methods) from PET from a bottle of daily life (from a local shop, Granini brand, nPET$_b$) and from a commodity thermoplastic polymer resin that is widely used for packaging (nonreheat PET resin RAMAPET N180, nPET$_c$), as well as from two PET products from GoodFellow Cambridge: biaxially oriented crystalline PET film (GoodFellow crystalline, nPET$_{GFc}$) and amorphous PET film (GoodFellow amorphous, nPET$_{GFa}$). According to the manufacturers, PET$_c$, PET$_{GFa}$ and PET$_{GFc}$ raw materials are of high purity (purity 99.9%), and the composition of PET$_b$ is according to legislation (Supplementary Note 4).

Using dynamic light scattering (DLS), the *Z*-average particle size (diameter) measured at 25 °C confirmed the presence of nPET particles with a stable, typical[18–20] size distribution from 53.1 ± 0.1 nm to 108.0 ± 0.1 nm (Fig. 5a, Extended Data Table 2 and Supplementary Data 7), which is in the sub-micro to nanometre range. By differential scanning calorimetry, the degree of crystallinity (%), T_G, melting temperature (T_m), cold crystallization temperature (T_c) and cold crystallization energy (ΔH_c) of the bulk PET materials and the nPET particles could be also obtained (Extended Data Table 2 and Supplementary Fig. 13). The crystallinity, T_G, T_m and T_c ranged from 1.3% to 34.5%, from 72.0 °C to 75.7 °C, from 245.9 °C to 251.9 °C, and from 192.8 °C to 215.1 °C, respectively, which is in the range of reported datasets[12,32,33]. For additional considerations, see Supplementary Note 5.

npFraC$_{m1}$ or npFraC$_{m2}$ were added at a concentration of 1.5 μg ml^{-1} (or 76 nM; Supplementary Note 6) to buffered suspensions (pH 7.0) containing 2.23 ± 0.06 mg ml^{-1} nPET$_{GFa}$, nPET$_{GFc}$, nPET$_b$ and nPET$_c$, and the degradation products were observed by high-performance liquid chromatography (HPLC) (Fig. 6a,b) after 48 h of incubation at T_{opt}, 40 °C. T_{opt} refers to the temperature at which maximal ester-hydrolytic activity was observed using *p*-NP propionate (Supplementary Fig. 11 and Supplementary Data 5); at this temperature, npFraC$_{m1}$ and npFraC$_{m2}$

https://doi.org/10.1038/s41929-023-01048-6

Table 1 | Kinetic hydrolysis parameters of ETE and $nPET_b$ for $npFraC_{m1}$ and $npFraC_{m2}$

Substrate	Kinetic hydrolysis parameters		
	$npFraC_{m1}$	$npFraC_{m2}$	LCC_{WT}
ETE[a]	K_m: 0.65±0.08 mM k_{cat}: 16.52±0.9 min^{-1} k_{cat}/K_m: 424 $M^{-1}s^{-1}$	K_m: 1.32±0.05 mM k_{cat}: 107.9±7.5 min^{-1} k_{cat}/K_m: 1,362 $M^{-1}s^{-1}$	Not determined
$nPET_b$[b]	$^{conv}K_m$: 0.59±0.28 g l^{-1} $^{conv}k_{cat}$: 91.2±0.1 min^{-1}	$^{conv}K_m$: 0.88±0.21 g l^{-1} $^{conv}k_{cat}$: 496±0.2 min^{-1}	$^{conv}K_m$: 0.42±0.04 g l^{-1} $^{conv}k_{cat}$: 12.2±0.5 min^{-1}
$nPET_b$[c]	$^{inv}K_m$: 13.2±7.3 μg g^{-1} $nPET_b$ $^{inv}k_{cat}$: 202.8±33.6 nM s^{-1}	$^{inv}K_m$: 47.2±1.2 μg mg^{-1} $nPET_b$ $^{inv}k_{cat}$: 13,263±256 nM s^{-1}	$^{inv}K_m$: 121.4±94.1 μg g^{-1} $nPET_b$ $^{inv}k_{cat}$: 4,492±1,768 nM s^{-1}
$nPET_b$[d]	Γ_{attack}: 0.12±0.03 μmol g^{-1} $nPET_b$	Γ_{attack}: 1.46±0.23 μmol g^{-1} $nPET_b$	Γ_{attack}: 20.1±1.6 μmol g^{-1} $nPET_b$

[a]Reaction conditions for K_m are listed as follows: [$npFraC_{m1/m2}$], 18.3 μg ml^{-1}; [**ETE**], 0–3.6 mM; reaction volume, 44 μl; reaction time, 10 min; *T*, 40 °C; pH, 8.0 (5 mM EPPS buffer); format: 384-well plates (ref. 781162, Greiner Bio-One GmbH). Reaction conditions for k_{cat} are listed as follows: [$npFraC_{m1}$ or $npFraC_{m2}$], 0–5.5 μM; [**ETE**], 20 mM (substrate saturation); reaction volume, 44 μl; *T*, 40 °C; pH, 8.0 (5 mM EPPS); format, 384-well plates (ref. 781162, Greiner Bio-One GmbH). Datasets were collected with a Synergy HT Multi-Mode Microplate reader (BioTek Instruments) with Gen5 2.00 software, with values obtained from the best linear fit using SigmaPlot 14.5. [b]Reaction conditions are listed as follows: [$npFraC_{m1}$], 15 μg ml^{-1}; [$npFraC_{m2}$], 30 μg ml^{-1}; [LCC_{WT}], 132 μg ml^{-1}; [$nPET_b$], 0–4.4 mg ml^{-1}; reaction volume, 50 μl; reaction time, 30 min (for $npFraC_{m1}$ and $npFraC_{m2}$) or 60 min (for LCC_{WT}); *T*, 40 °C; pH, 7.0 (20 mM HEPES buffer); 1,000 rpm. [c]Reaction conditions are listed as follows: [$npFraC_{m1}$], 0–73 μg g^{-1} $nPET_b$; [$npFraC_{m2}$], 0–118 μg g^{-1} $nPET_b$; [LCC_{WT}], 0–118 μg g^{-1} $nPET_b$; [$nPET_b$], 1.1 g l^{-1}; reaction volume, 50 μl; *T*, 40 °C; pH, 7.0 (20 mM HEPES buffer); agitation, 1,000 rpm; time of reaction, 30 min ($npFraC_{m1/m2}$) or 60 min (LCC_{WT}). The reactions[b,c] were stopped by diluting ten times with dimethyl sulfoxide (from Merck Life Science) and immediately analysed by HPLC. Datasets were collected with a Varian Star LC workstation 6.41 (Varian), with values obtained from the best linear fit using SigmaPlot 14.5. Values are plotted as the mean of three independent replicates ($n=3$) with the reported error ranges and standard deviations (s.d.) calculated using the STDEV.S function in Excel 2019 (calculations and raw data are provided in Source Data). Raw data and calculations are shown in Supplementary Data 4, 12 and 13. [d]Calculated according to Bååth et al.[31]. **ETE** is highlighted in bold as this is not a standard nomenclature of a chemical product but an abbreviation, according to Schubert et al.[29].

retained 54.7 ± 2.1% and 32.7 ± 6.3%, respectively, of their original activities after 48 h (Supplementary Fig. 14 and Supplementary Data 8). The chemical structures of all degradation products identified under our assay conditions are detailed in Extended Data Fig. 1. The identity was confirmed by high-resolution mass spectrometry (MS) analysis using products purified from reaction mixtures by semipreparative HPLC (Supplementary Fig. 15).

The HPLC chromatograms in Fig. 6a revealed four main degradation products when nPET particles were treated with $npFraC_{m1}$: **ETE**, **ETETE**, **TE** and **TETETE**, in this order, with **T** being below the detection limit under our assay conditions. This substrate profile was markedly different from that of $npFraC_{m2}$, which yields a higher diversity of oligomers, herein referred to as **TET**, **TETE**, **TETET** and **TETETE**, in addition to **T**, **TE** and **ETE** (Fig. 6b). Under the same experimental conditions, *Is*PETase, LCC_{WT} and LCC_{WCCG} released **T**, **TE**, **ETE** and the oligomers **TET**, **TETE** and/or **TETETE**, with **T** and **TE** being the main degradation products (Extended Data Fig. 2a–c); the presence of these products is in accordance with the literature and reaction mechanisms[15,34]. However, **TET** was not detected or suggested as a potential degradation product during the degradation of PET film by *Is*PETase[34].

According to calibration with pure standards (**T**, **TE**, **ETE**, **TET**, **TETE** and **ETETE**), the concentration of degradation products at 48 h using $npFraC_{m1}$ ranged from 1,718 to 5,743 μM, depending on the type of nPET (Fig. 6c and Supplementary Data 9), with $nPET_{GFa}$ and $nPET_{GFc}$ being degraded to a higher extent than $nPET_b$ and $nPET_c$, despite their higher crystallinity. In all cases, **ETE** was the major degradation product, whose concentration ranged from 2.1- to 12.5-fold higher than that of **TE**, depending on the type of nPET. When $npFraC_{m2}$ was used, the concentration of degradation products at 48 h ranged from 1,500 to 2,660 μM, depending on the type of nPET, with $nPET_b$ and $nPET_{GFa}$ being the preferred particles, and **TE** was produced at approximately 3-fold higher concentrations than **ETE** (Fig. 6d and Supplementary Data 9). *Is*PETase, LCC_{WT} and LCC_{WCCG} released degradation products at concentrations of 1,154–1,884 μM, 312–410 μM and 309–414 μM, respectively, depending on the type of nPET (Extended Data Fig. 2d–f and Supplementary Data 9). In all cases, **T** was observed, and **TE** was found to have a concentration 6- to 31-fold higher than **ETE**, depending on the nPET and the PETase. The higher efficiency of *Is*PETase compared with LCC_{WT} and LCC_{WCCG} could be associated with the higher activity of this enzyme at 40 °C compared with LCC variants[17,18].

This finding confirmed the capacity of $npFraC_{m1}$ and $npFraC_{m2}$ to efficiently deconstruct nPET materials at 40 °C. The uniqueness of $npFraC_{m1}$ compared with the $npFraC_{m2}$, *Is*PETase and $LCC_{WT/WCCG}$ variants in degrading nPET is that **ETE** is the main degradation product compared with **TE**, with no appreciable formation of **T** under our assay conditions. This feature could represent an advantage over the other enzymatic systems that will produce a mixture of **E**, **T**, **TE** and **ETE**.

Time course and kinetic study of $nPET_b$ particle degradation

The time course of the released degradation products, determined by HPLC using $npFraC_{m1}$ and $npFraC_{m2}$, was followed and compared with that of LCC_{WT} at 40 °C and pH 7.0. $nPET_b$ (diameter 108.0 ± 0.1 nm; Extended Data Table 2) was targeted as the closest example to real nPET substrates, and all three enzymatic preparations were able to efficiently degrade it. Although, *Is*PETase is currently the most active wild-type enzyme for PET hydrolysis at around 40 °C, LCC_{WT} was selected for comparative purposes as a benchmark PETase given its higher stability compared with mesophilic *Is*PETase under our thermal assay conditions, of 40 °C (for details, see Supplementary Note 7; Supplementary Fig. 16 and Supplementary Data 11).

As shown in Fig. 7 (Supplementary Data 10), degradation products were constantly observed since the early stages for the three enzymatic preparations. Under the tested assay conditions, the time course of degradation product release was much steeper with $npFraC_{m2}$ than with $npFraC_{m1}$ in the first few reaction hours. Whereas $npFraC_{m2}$ was only highly active until 5–6 h of incubation, hydrolysis by $npFraC_{m1}$ continuously progresses up to 24 h where almost maximal depolymerization was achieved, as for LCC_{WT} for which hydrolysis progressed beyond 24 h. This is consistent with the lower thermal stability of $npFraC_{m2}$ ($t_{1/2}$ at 40 °C: 5.3 ± 0.2 h) compared with $npFraC_{m1}$ ($t_{1/2}$ at 40 °C > 48 h) under the assay conditions (Supplementary Fig. 14 and Supplementary Data 8). Additionally, the better positioning of the long protuberances that conformed the nPET particles (Discussion) in the nanopore channel once the particle is seated at the pore entrance, could also explain the differences in the reaction kinetics and dynamics of $npFraC_{m1}$ and $npFraC_{m2}$. Regardless of the underlying reasons for a different kinetics, these data demonstrate that the access of nPET particles across the nanopores is not a limiting factor during depolymerization mediated by $npFraC_{m1}$ and $npFraC_{m2}$.

To evaluate the effect of the particle size, we prepared $nPET_b$ particles of different mean sizes (diameter), namely from 69.1 ± 0.8 to 153.8 ± 1.4 nm (Fig. 5b and Supplementary Data 7). We discovered that smaller particles were hydrolysed by $npFraC_{m1}$ more easily than larger particles (Fig. 5c), whereas $npFraC_{m2}$ preferred particles from 85.4 to 108 nm (Fig. 5d), in accordance with the increased exposure of its active site to the particles (Fig. 4). These data suggest that, while particles as large as 153.8 nm were degraded (from 8.0- to 4.4-fold lower than that of the best performing size), there will be a particle size limit that will most likely no longer be degraded. Regardless of this finding, the analysed particle sizes are well above the $npFraC_{m1}$ and $npFraC_{m2}$ sizes, namely 6.7 nm in the *cis* entry and 1.9 nm in the *trans* exit[21] (Fig. 4).

The results of the conventional (^{conv}MM) and inverse (^{inv}MM) Michaelis–Menten kinetics[35] are summarized in Supplementary Fig. 17a–f (Supplementary Data 12 and 13), and the parameters resulting from the fits (pH 7.0, 40 °C) are presented in Table 1. The results highlight that the affinity, deconstruction rates and reactive site density

https://doi.org/10.1038/s41929-023-01048-6

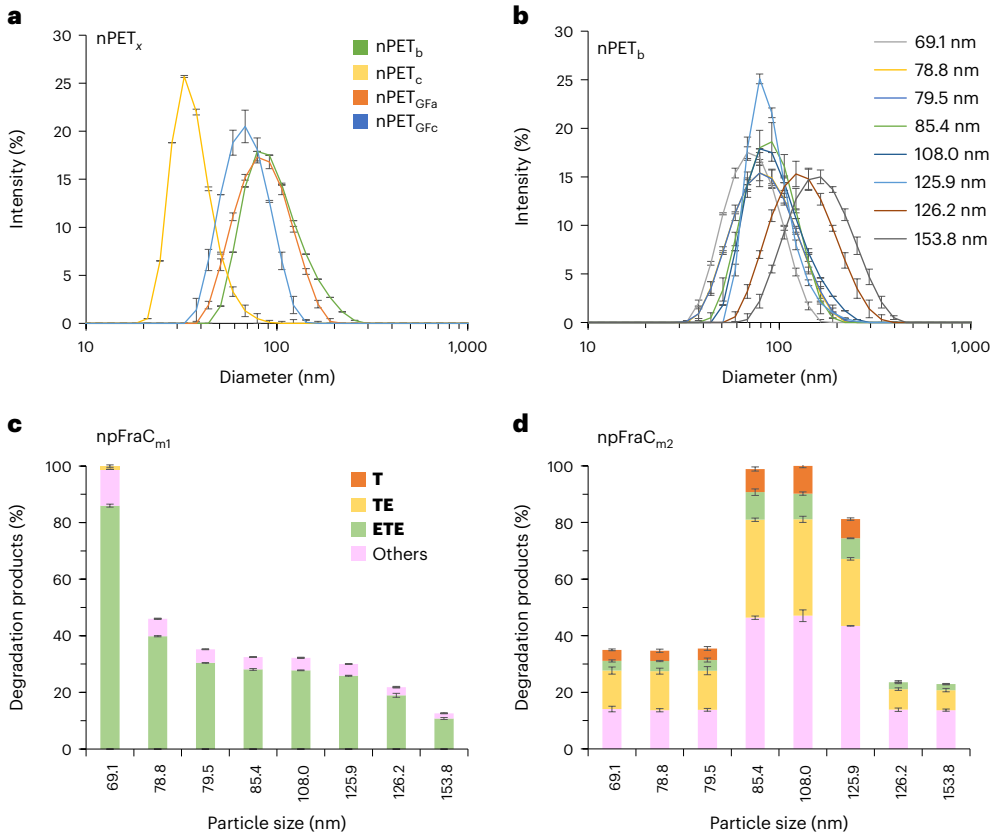

Fig. 5 | Particle size distribution of nPET$_{GFa/GFc/b/c}$ as determined by DLS. a,**b**, The distribution mean (Dv,50) size (±s.d. error bar) calculated by the scattered intensity for each particle size from three measurements ($n = 3$) is represented (**a**, for nPET$_x$ where x refers to GFa/GFc/b/c; **b**, for nPET$_b$ obtained at various transfer rates). Particles were obtained by predissolving PET$_b$ for 2 h at 150 rpm and 25 °C in 1,1,1,3,3,3-hexafluor-2-propanole (from Merck Life Science) and further transferred with the help of a burette into an ice-cold water-containing beaker (in an ice bath), which was strongly agitated (250 rpm). For **a**, the flow rate was fixed at 1 ml min^{-1}, and for **b**, it was fixed at 0.05, 0.10, 0.25, 0.5, 1.0, 1.5 and 2.0 ml min^{-1} for producing 69.1, 78.8, 79.5, 85.4, 108.0, 125.9, 126.2 and 153.8 nm particles, respectively (Supplementary Methods). DLS datasets were collected at 25 °C with a Malvern Instrument (MALVERN ZETASIER NANO S ZEN 1600, IESMAT) with Dispersion Technology software 4.20 (Malvern Instrument). **c**, Evaluation of the degradation of nPET$_b$ particles of different sizes using npFraC$_{m1/m2}$. Reaction conditions: [npFraC$_{m1/m2}$], 1.5 μg ml^{-1}; [nPET$_b$], 1.1 mg ml^{-1}; reaction volume, 100 μl; T, 40 °C; pH, 7.0 (20 mM HEPES buffer); reaction time, 48 h. The reactions were maintained in 2-ml safe-lock Eppendorf polypropylene tubes (ref. 0030 120.094) in a thermoshaker (model Thermomixer comfort, Eppendorf AG) at 1,000 rpm. The reactions were stopped by adding 900 μl dimethyl sulfoxide (from Merck Life Science), and the degradation products were immediately analysed by HPLC. Datasets were collected with a Varian Star LC workstation 6.41 (Varian). Quantifications of degradation products were performed by HPLC on the basis of calibrations with purified standards. Values in **a** and **b** are plotted as the mean of three independent replicates ($n = 3$) with the reported error ranges and s.d. calculated using Dispersion Technology software 4.20 (Malvern Instrument). Values in **c** and **d** are plotted as the mean of three independent replicates ($n = 3$) with the reported error ranges and s.d. calculated using the STDEV.S function in Excel 2019 (calculations and raw data are provided in Source Data). The figure was made using Excel 2019. Raw data are shown in Supplementary Data 7.

(Γ_{attack}) of the catalytic nanopores are comparable to those of soluble PETases, demonstrating that having a catalytic unit in a nanopore does not substantially affect either the affinity for, or the reaction rate towards, the nPET particles, as well as the concentration of reactive sites available per gram of substrate compared with a soluble enzyme with free access to the particles. For additional kinetic details, see Supplementary Note 7.

Morphological evolution during nPET$_b$ degradation by npFraC$_{m1}$ and npFraC$_{m2}$

The change in particle size distribution and morphology was analysed by field emission scanning electron microscopy (FE-SEM) in dried samples collected before, during and after hydrolysis. The FE-SEM micrographs in Supplementary Fig. 18 (Source Data) show the morphological degradation of the nPET$_b$ particles by npFraC$_{m1}$ and npFraC$_{m2}$. The as-synthesized spheres, with a relatively uniform size distribution, start aggregating and degrading after few minutes of hydrolysis, appearing covered by a film of insoluble degradation products in the samples incubated with npFraC$_{m1/m2}$. Eventually, all particles disappeared and only large aggregates of degradation products are visible, as observed for PETases with a random-hydrolysis mechanism[20].

Discussion

This study focused on the design of two pore-based biocatalytic nanoreactors for nPET particle depolymerization, using a non-catalytic pore-forming protein as the starting target. Through a combination of computational structure-based modelling tools and different experimental techniques, we provide robust datasets demonstrating that these biocatalytic nanopores can break down primary nPET of different types at 40 °C. The diameter of the nPET particles produced and tested ranged from approximately 53 to 154 nm, whereas the FraC pore has an inner diameter ranging from 1.9 nm (*cis* exit) to 6.7 nm (*trans* exit)[21]. Therefore, if we stick with this static image, one might suggest that nPET particles would not be able to access the artificial active centres introduced into the nanopores, although experimental evidence shows otherwise. Since the entry of each particle in its entirety into the pore would not be possible, we propose that the nPET particles may have protuberances and that it is not the particles that enter into the nanopores but the protuberances (Fig. 4),

https://doi.org/10.1038/s41929-023-01048-6

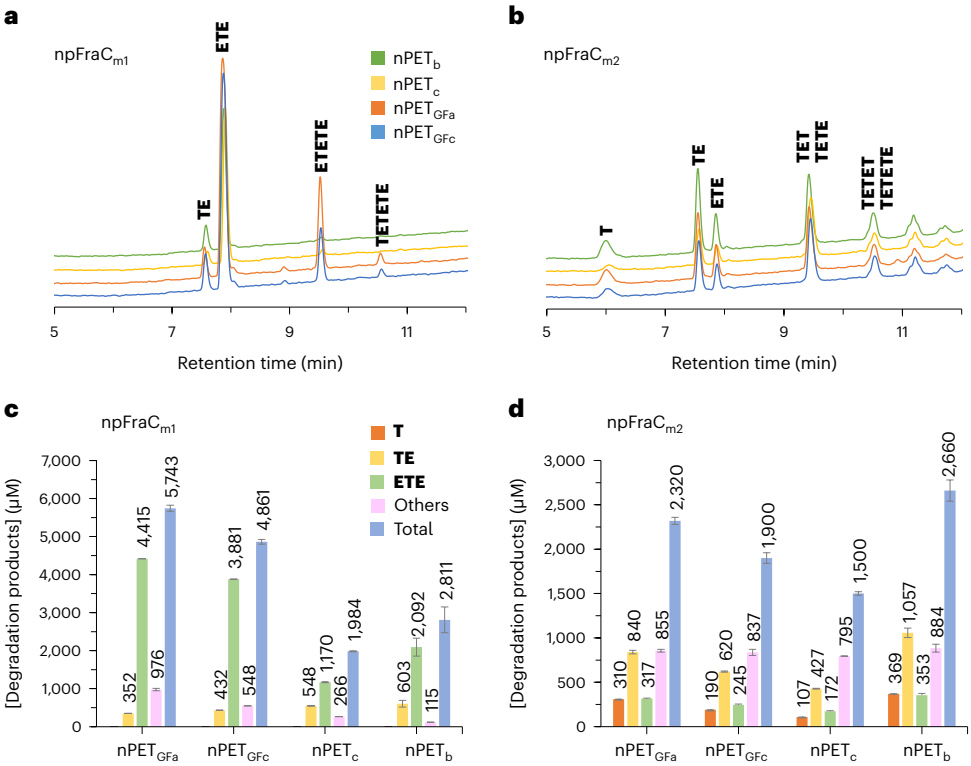

Fig. 6 | Degradation profiles of nPET$_{GFa/GFc/b/c}$ treated with npFraC$_{m1/m2}$. **a**,**b**, HPLC profiles of degradation products released by npFraC$_{m1}$ (**a**) or npFraC$_{m2}$ (**b**) under the experimental conditions: [npFraC$_{m1/m2}$], 1.5 μg ml^{-1}; [nPET$_{GFa/GFc/b/c}$], 1.1 mg ml^{-1}; reaction volume, 1,000 μl; *T*, 40 °C; pH, 7.0 (20 mM HEPES buffer); reaction time, 48 h. The reactions were maintained in 2-ml safe-lock Eppendorf polypropylene tubes (ref. 0030 120.094) in a thermoshaker (model Thermomixer comfort, Eppendorf AG) at 1,000 rpm. Aliquots of 100 μl were obtained, the reactions were stopped by adding 900 μl dimethyl sulfoxide (from Merck Life Science) and the degradation products were immediately analysed by HPLC. Datasets were collected with a Varian Star LC workstation 6.41 (Varian). All reactions and analyses were performed in triplicate (*n* = 3), with a representative chromatogram per enzyme and nPET particle shown. **c**,**d**, Concentration of degradation products found to be present in reaction mixtures with npFraC$_{m1}$ (**c**) or npFraC$_{m2}$ (**d**). Quantification was performed for products shown in **a** and **b** with unambiguous identification and for which enough material was recovered for HPLC calibration, namely from **T** to **ETETE** (Extended Data Fig. 1); purification was performed by semipreparative HPLC, and the molecular weights and structures were determined by mass spectrometry (Supplementary Fig. 15). Values are plotted as the mean of three independent replicates (*n* = 3) with the reported error ranges and s.d. calculated using the STDEV.S function in Excel 2019 (calculations and raw data are provided in Source Data). The figure was constructed using Excel 2019. Raw data are shown in Supplementary Data 9.

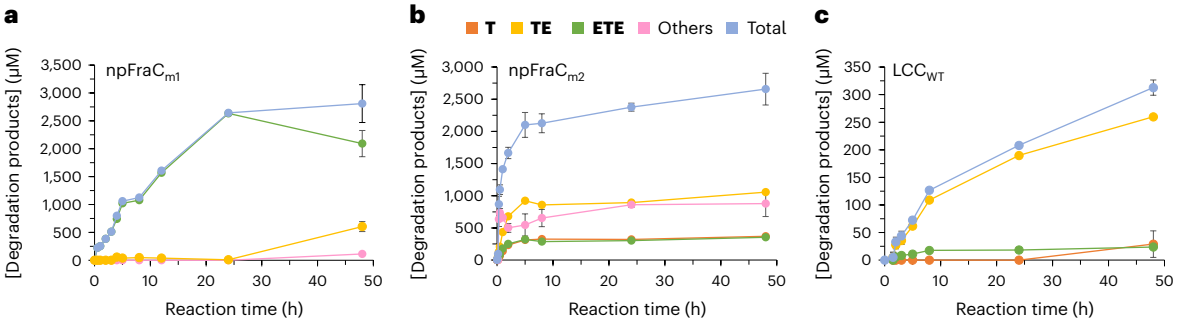

Fig. 7 | Time course study of nPET$_b$ degradation using npFraC$_{m1/m2}$ compared with LCC$_{WT}$. **a**–**c**, Time course degradation of nPET$_b$ particles using npFraC$_{m1}$ (**a**), npFraC$_{m2}$ (**b**) and LCC$_{WT}$ (**c**). Reaction conditions and dataset collections are detailed in Figs. 5 and 6, and Extended Data Fig. 2. In brief: 1.1 mg ml^{-1} nPET$_b$, 1.5 μg ml^{-1} npFraC$_{m1/m2}$, LCC$_{WT}$, 40 °C, pH 7.0. Values are plotted as the mean of three independent replicates (*n* = 3) with the reported error ranges and s.d. calculated using the STDEV.S function in Excel 2019 (calculations and raw data are provided in Source Data). Raw data are provided in Supplementary Data 10.

the size of which will be reduced during hydrolysis, and with it the size of the particles, that will be more accessible as the hydrolysis proceeds. This may agree with the fact that the molecular weight of sub-micro- and nano-sized PET particles may be lower compared with that of the pristine materials, and that the degradability of sub-micrometre particles and nanoparticles may not only be due to the increased surface area, but also to the lower chain lengths and more flexible polymer chain ends[36].

The data suggest that npFraC$_{m1}$ performs endo-hydrolysis on the small protuberances that can access the internal area of the catalytic nanopore; this would result in the generation of **E** (^{E}PET) and **T** (or ^{T}PET) terminal PET oligomers, from which smaller subproducts, preferentially **ETE** and **ETETE** (from ^{E}PET), and to a lesser extent **TETETE** (from ^{T}PET), will be formed by exo-type chain scission. In the case of npFraC$_{m2}$, the active site is remarkably more exposed to the solvent

and to different accommodations of the sub-micro- and nanoparticles (and of its protuberances), initiating a more random endo- and exo-type chain degradation that yields a high diversity of oligomers and monomers. The high accumulation of all such degradation products (Fig. 6) suggests that the cleavage of ^{T}PET and ^{E}PET by npFraC$_{m2}$ would occur at similar rates. This finding contrasts with the PET degradation process proposed for *Is*PETase, where the terminal digestion step of ^{T}PET is preferred[34].

Compared with benchmark PETases, namely LCC$_{WT}$, LCC$_{WCCG}$ and *Is*PETase, we discovered remarkable differences in hydrolysis capacity and degradation products (Extended Data Fig. 3). Under our experimental conditions, npFraC$_{m1}$ breaks down nPET to **ETE** as the main degradation product without appreciable production of **T**, which is a final PET-building block that is usually produced by the benchmark PETases[12–20,34]. Instead, npFraC$_{m2}$ behaves similarly to benchmark PETases in the sense that it can fully convert nPET to **T**, but unlike them, it produces a greater diversity of degradation products. The possibility of using FraC to design two catalytic nanopores capable of degrading nPET at relatively low temperatures (40 °C) and with different degradation profiles among them and compared with benchmark PETases demonstrates the versatility of this protein as a scaffold for the design of pore-based catalytic nanoreactors to deconstruct nPET particles. Note that up to eight refined artificial biocatalytic sites could be incorporated due to the homo-octamer assembly. Therefore, the limitations in the access of the nPET particles to the active sites can be compensated by the presence of multiple catalytic groups, whose number would be higher than in conventional enzymes with PETase activity. Indeed, our results demonstrated that, using the same conditions and particles, and considering the limitations of access to the particles, the catalytic efficiency for nPET$_{b}$ of npFraC$_{m1}$ and npFraC$_{m2}$ is similar to that of soluble LCC$_{WT}$[15].

The above features, with the easy production, simple purification and stability of the engineered catalytic nanopores designed herein (Supplementary Note 2), can create new alternatives to degrade sub-micro- and nano-sized PET, for example, in wastewater treatment plants[18], under sustainable conditions, for example, 40 °C. The proof of concept presented in this study may open up new lines of research. We envision, for example, the co-integration of the two artificial hydrolytic sites or designing thermostable variants by further protein engineering efforts to have robustness above 70 °C to degrade real-world plastic pollution at an industrially relevant scale[18]. Also, the co-integration of engineered pore-forming proteins and nanoscale materials or membranes to develop inorganic–organic hybrid catalysts that can act as both filtering systems to effectively capture sub-micro- and nano-sized PET, mimicking the well-known water desalination nanopores[37], and reaction chambers to further degrade synthetic particles[38] (Supplementary Note 9). The possibility of producing engineered transmembrane pore-forming proteins, which include FraC or other larger pore-forming proteins that can oligomerize in annular pores of more than 30 monomers and large diameters (for example, the 25–40 nm Perfringolysin O[39]), in target cell membranes may also enable the design of microbial reactors with integrated catalytic pores supporting multiple conversions, yet to be defined, as exemplified here by nPET degradation.

Methods

In silico protein and substrate preparation

We selected the homo-octamer biological assembly crystal structure of FraC (4TSY[40]) and its monomer soluble structure (3W9P[41]). Each system was prepared and optimized at pH 7.5 with a Protein Preparation Wizard[42] from Schrodinger to fix the protonation states and correct alternative positions or other common problems. The three model esters (Supplementary Fig. 1), **TE** and **ETE** were modelled using the OPLS2005 force field[43], and the atomic charges were obtained using single-point energy quantum mechanics calculations with density functional theory using the B3LYP-D3 exchange-correlation and CC-PVTZ basis set.

PELE, adaptive simulations and distance metrics

The engineering protocol starts by mapping possible substrate binding sites in the target protein. Interactions between the different ester-type substrates and the inner surface of the assembled pore-forming protein scaffold were thus sampled using PELE software[44]. Through a PELE Global Exploration, we obtained an energy landscape profile. Further, in PELE Local Exploration, we analysed the energy landscape profile with respect to the catalytic distance between substrate ester reactive atoms and the nucleophile oxygen of the catalytic serine. Moreover, we estimated the relative activity of the active site for each substrate, calculating the number of catalytic events (equation (1)). The number of catalytic events for each substrate was determined by multiple substrate-active site distance metrics. The FraC$_{m1}$ contains eight possible combinations of serine–histidine interactions between α-helices and two equidistant acids that can complete the catalytic triad, increasing the possible combinations. To avoid underestimation of catalytic events, we generated a distance matrix for each PELE step for all active sites and selected the catalytic triad nearest the substrate. For FraC$_{m2,}$ we focused on only one monomer globular part. For extensive details, see Supplementary Methods.

$$\mathrm{NRA} = \frac{\text{number of catalytic PELE poses}}{\text{total number of accepted PELE steps} \times \text{number of ester groups}}\% \quad (1)$$

MD simulations of FraC$_{m1}$, FraC$_{m2}$ and the polymer

To analyse the stability of the membrane-inserted N-terminal domains in FraC$_{m1/m2}$, MD simulations were performed using the Bilayer Membrane Builder protocol with the replacement method provided by CHARMM-GUI[45] and GROMACS 5.1.2 simulations[46]. To analyse the MD of the polymer, including its flexibility in the solvent of a 200-monomer PET fragment, MD simulations were performed using the Polymer Builder protocol provided by CHARMM-GUI[45] and GROMACS 5.1.2 (ref. 46). To obtain the different metrics of all MD simulations, the MDTraj[47] and MDAnalysis[48] Python modules were employed. For the simulation of the polymer, we used GROMACS[49] analysis tools to obtain its solvent-accessible surface area. For extensive details, see Supplementary Methods.

QM/MM minimizations

QM/MM minimizations of the reactant state in *Is*PETase, FraC$_{m1}$ and FraC$_{m2}$ mutants were performed using Qsite from the Schrödinger Suite[50]. The calculations were performed at the DFT/B3LYP and 6-31G* basis set level of theory. The QM region included **ETE** as a substrate and catalytic serine and histidine residues: Ser131 and His208 for *Is*PETase, Ser21 and His20 for FraC$_{m1}$ and Ser38 and His175 for FraC$_{m2}$. The *Is*PETase reactant state's structure was based on the PDB code 5XH3 (ref. 51), and both FraC mutant structures were based on a catalytic PELE pose.

npFraC$_{WT}$, npFraC$_{m1}$ and npFraC$_{m2}$ production and assembly

The complementary DNA encoding FraC$_{m1}$, with Lys20His/Thr21Ser mutations, and FraC$_{m2}$, with Asp38Ser/Glu173Gln mutations, were obtained via the overlap extension mutagenesis method[22,52]. FraC$_{WT}$, FraC$_{m1}$ and FraC$_{m2}$ were produced in an *E. coli* expression system and purified as previously described[21,22]. Pore assembly was performed to mimic the actual situation encountered by actinoporins in nature, as detailed in Supplementary Methods.

LCC$_{WT}$, LCC$_{WCCG}$ and *Is*PETase: source and purification

The genes coding for the cutinase LCC in its wild-type form (LCC$_{WT}$)[18], as well as the WCCG variant (LCC$_{WCCG}$)[19], were codon-optimized for *E. coli* K12 and synthesized by Biomatik in pET21a(+) (Novagen) between the restriction sites NdeI and SalI and were kindly donated by Pablo Pérez-García (Universität Hamburg, Germany). The construct containing the gene coding for *Is*PETase fused to a maltose-binding protein in

the backbone of pMAL-p4x was kindly donated by Sebastian Weigert (University of Bayreuth, Germany)[20]. The proteins were produced and purified as reported and stored at 1.5 mg ml^{-1} in 40 mM HEPES buffer pH 7.0 until use.

Sub-micro- and nano-sized PET degradation tests: time course and kinetics

For the nPET$_b$, nPET$_c$, nPET$_{GFa}$ and nPET$_{GFc}$ degradation tests, the following conditions were utilized, if otherwise not indicated: [npFraC$_{m1/m2}$, *Is*PETase and LCC$_{WT/WCCG}$], 1.5 μg ml^{-1}; [nPET$_{GFa/GFc/b/c}$], 1.1 mg ml^{-1}; reaction volume, 1,000 μl; *T*, 40 °C; pH, 7.0 (20 mM HEPES buffer); reaction time, 48 h. For conventional Michaelis–Menten kinetic analysis, reaction conditions are listed as follows: [npFraC$_{m1}$], 15 μg ml^{-1}; [npFraC$_{m2}$], 30 μg ml^{-1}; [LCC$_{WT}$], 132 μg ml^{-1}; [nPET$_b$], 0.38–4.4 mg ml^{-1}; reaction volume, 50 μl; reaction time, 30 min (for npFraC$_{m1}$ and npFraC$_{m2}$) or 60 min (for LCC$_{WT}$); *T*, 40 °C; pH, 7.0 (20 mM HEPES buffer); 1,000 rpm. For inverse Michaelis–Menten kinetic analysis, the following reaction conditions were used: [npFraC$_{m1}$], 0–73 μg g^{-1} nPET$_b$; [npFraC$_{m2}$], 0–118 μg g^{-1} nPET$_b$; [LCC$_{WT}$], 0–118 μg g^{-1} nPET$_b$; [nPET$_b$], 1.1 g l^{-1}; reaction volume, 50 μl; *T*, 40 °C; pH, 7.0; agitation, 1,000 rpm; time of reaction, 30 min (for npFraC$_{m1}$ and npFraC$_{m2}$) or 60 min (for LCC$_{WT}$). Evaluation of the degradation of nPET$_b$ particles of different sizes using npFraC$_{m1/m2}$ was performed using the following reaction conditions: [npFraC$_{m1/m2}$], 1.5 μg ml^{-1}; [nPET$_b$], 1.1 mg ml^{-1}; reaction volume, 100 μl; *T*, 40 °C; pH, 7.0 (20 mM HEPES buffer); reaction time, 48 h. All reactions were maintained in 2-ml safe-lock Eppendorf polypropylene tubes (ref. 0030 120.094; Eppendorf AG) in a thermoshaker (model Thermomixer comfort, Eppendorf AG). The reactions were stopped, at the indicated times, by diluting ten times with dimethyl sulfoxide (from Merck Life Science) and the degradation products were immediately analysed by HPLC (Supplementary Methods). In all cases, datasets were collected with a Varian Star LC workstation 6.41 (Varian) and analysed using Excel 2019 and SigmaPlot 14.5. Quantifications of degradation products were performed by HPLC on the basis of calibrations with purified standards, whose identity was confirmed by high-resolution MS (see raw MS data in Supplementary Data 14). All reactions were performed in triplicate (n = 3) with the following control reactions set up using the same amount of material: (1) soluble FraC$_{WT}$, FraC$_{m1}$ and FraC$_{m2}$; (2) npFraC$_{WT}$; (3) no protein; and (4) nPET$_b$, nPET$_c$, nPET$_{GFa}$ and nPET$_{GFc}$, without protein added.

Ester hydrolysis assays

The hydrolysis of glyceryl tripropionate (ref. W328618), vinyl acetate (ref. V150-3), phenyl acetate (ref. 108723), **ETE** (ref. 465151), from Merck Life Science, and **TE** (purified as detailed in Supplementary Methods) was assayed using a pH indicator assay at 40 °C and pH 8.0 by monitoring the absorbance at 550 nm (extinction coefficient (ε) of phenol red, 8,450 M^{-1} cm^{-1}), as reported[26,27]. The hydrolysis of the model esters *p*-NP acetate (ref. N-8130; Merck Life Science), propionate (Santa Cruz Biotechnology, ref. sc-256813) and butyrate (ref. N-9876; Merck Life Science) was assessed by monitoring the continuous production of 4-nitrophenol at 348 nm (pH-independent isosbestic point, ε = 4,147 M^{-1} cm^{-1})[26]. In all cases, a Synergy HT Multi-Mode Microplate Reader with Gen5 2.00 software (Biotek Instruments) was used. All reactions were performed in triplicate (n = 3) with control reactions and background signals considered, as reported[26,27]. For extensive details, see Supplementary Methods.

Reporting summary

Further information on research design is available in the Nature Portfolio Reporting Summary linked to this article.

Data availability

The authors declare that the main data supporting the findings of this study are available within the paper and related Supplementary Information, Supplementary Data and Source Data files. The molecular simulations, the MD simulations and the quantum mechanical minimizations have been deposited at Zenodo (https://zenodo.org/deposit/7755566)[53] under the identifier https://doi.org/10.5281/zenodo.7755566. To use the archive, download the file and extract its contents to a local directory using appropriate software. The directory contains separate folders for each type of simulation, along with input, output and README files. Source data are provided with this paper (the mass spectrometry files can be analysed with the software MassLynx V4.1). All other data are available from the authors upon reasonable request.

References

1. York, A. Adapting to plastic.*Nat. Rev. Microbiol.* **18**, 362–363 (2020).
2. Rosenboom, J. G., Langer, R. & Traverso, G. Bioplastics for a circular economy. *Nat. Rev. Mater.* **7**, 117–137 (2022).
3. Geyer, R., Jambeck, J. R. & Law, K. L. Production, use, and fate of all plastics ever made. *Sci. Adv.* **3**, e1700782 (2017).
4. Cabernard, L. et al. Growing environmental footprint of plastics driven by coal combustion. *Nat. Sustain.* **5**, 139–148 (2022).
5. Jambeck, J. R. et al. Marine pollution. Plastic waste inputs from land into the ocean. *Science* **347**, 768–771 (2015).
6. Gigault, J. et al. Current opinion: what is a nanoplastic? *Environ. Pollut.* **235**, 1030–1034 (2018).
7. Allen, S. et al. Atmospheric transport and deposition of microplastics in a remote mountain catchment. *Nat. Geosci.* **12**, 339–344 (2019).
8. Schymanski, D. et al. Analysis of microplastics in drinking water and other clean water samples with micro-Raman and micro-infrared spectroscopy: minimum requirements and best practice guidelines. *Anal. Bioanal. Chem.* **413**, 5969–5994 (2021).
9. Materić, D. et al. Nanoplastics measurements in Northern and Southern polar ice. *Environ. Res.* **208**, 112741 (2022).
10. Wei, R., Bertling, J., O'Connor, K., Bank, L. M. & Bornscheur, U. T. Possibilities and limitations of biotechnological plastic degradation and recycling. *Nat. Catal.* **3**, 867–871 (2020).
11. Ellis, L. D. et al. Chemical and biological catalysis for plastics recycling and upcycling. *Nat. Catal.* **4**, 539–556 (2021).
12. Wei, R. et al. Mechanism-based design of efficient PET hydrolases. *ACS Catal.* **12**, 3382–3396 (2022).
13. Son, H. F. et al. Rational protein engineering of thermo-stable PETase from *Ideonella sakaiensis* for highly efficient PET degradation. *ACS Catal.* **9**, 3519–3526 (2019).
14. Bell, E. L. et al. Directed evolution of an efficient and thermostable PET depolymerase. *Nat. Catal.* **5**, 673–681 (2022).
15. Tournier, V. et al. An engineered PET depolymerase to break down and recycle plastic bottles. *Nature* **580**, 216–219 (2020).
16. Lu, H. et al. Machine learning-aided engineering of hydrolases for PET depolymerization. *Nature* **604**, 662–667 (2022).
17. Yoshida, S. et al. A bacterium that degrades and assimilates poly(ethylene terephthalate). *Science* **351**, 1196–1199 (2016).
18. Cui, Y. et al. Computational redesign of a PETase for plastic biodegradation under ambient condition by the GRAPE strategy. *ACS Catal.* **11**, 1340–1350 (2021).
19. Barth, M. et al. Effect of hydrolysis products on the enzymatic degradation of polyethylene terephthalate nanoparticles by a polyester hydrolase from *Thermobifida fusca*. *Biochem. Eng. J.* **93**, 222–228 (2015).
20. Vogel, K. et al. Enzymatic degradation of polyethylene terephthalate nanoplastics analyzed in real time by isothermal titration calorimetry. *Sci. Total Environ.* **773**, 145111 (2021).
21. Tanaka, K., Caaveiro, J. M. M., Morante, K., González-Mañas, J. M. & Tsumoto, K. Structural basis for self-assembly of a cytolytic pore lined by protein and lipid. *Nat. Commun.* **6**, 1–11 (2015).

22. Alegre-Cebollada, J. et al. Silent mutations at the 5′-end of the cDNA of actinoporins from the sea anemone *Stichodactyla helianthus* allow their heterologous overproduction in *Escherichia coli*. *J. Biotechnol.* **127**, 211–221 (2007).
23. Wloka, C., Mutter, N. L., Soskine, M. & Maglia, G. Alpha-helical Fragaceatoxin C nanopore engineered for double-stranded and single-stranded nucleic acid analysis. *Angew. Chem. Int. Ed. Engl.* **55**, 12494–12498 (2016).
24. Versloot, R. C. A. et al. Quantification of protein glycosylation using nanopores. *Nano Lett.* **22**, 5357–5364 (2022).
25. Roda, S., Robles-Martín, A., Xiang, R., Kazemi, M. & Guallar, V. Structural-based modeling in protein engineering. A must do. *J. Phys. Chem. B* **125**, 6491–6500 (2021).
26. Alonso, S. et al. Genetically engineered proteins with two active sites for enhanced biocatalysis and synergistic chemo- and biocatalysis. *Nat. Catal.* **3**, 319–328 (2020).
27. Roda, S. et al. A Plurizyme with transaminase and hydrolase activity catalyzes cascade reactions. *Angew. Chem. Int. Ed. Engl.* **61**, e202207344 (2022).
28. Mesa-Galloso et al. Disrupting a key hydrophobic pair in the oligomerization interface of the actinoporins impairs their pore-forming activity. *Protein Sci.* **26**, 550–565 (2017).
29. Schubert, S. et al. Reaction pathways for the enzymatic degradation of poly(ethylene terephthalate): What characterizes an efficient PET-hydrolase? *ChemBioChem* **24**, e202200516 (2023).
30. Jerves, C. et al. Reaction mechanism of the PET degrading enzyme PETase studied with DFT/MM molecular dynamics simulations. *ACS Catal.* **11**, 11626–11638 (2021).
31. Bååth, J. A., Borch, K., Jensen, K., Brask, J. & Westh, P. Comparative biochemistry of four polyester (PET) hydrolases. *ChemBioChem* **22**, 1627–1637 (2021).
32. Menzel, T. et al. Impact of enzymatic degradation on the material properties of poly(ethylene terephthalate). *Polymers* **13**, 3885 (2021).
33. Bashir, Z., Al-Aloush, I., Al-Raqibah, I. & Ibrahim, M. Evaluation of three methods for the measurement of crystallinity of pet resins, preforms, and bottles. *Polym. Eng. Sci.* **40**, 2442–2455 (2000).
34. Joo, S. et al. Structural insight into molecular mechanism of poly(ethylene terephthalate) degradation. *Nat. Commun.* **9**, 382 (2018).
35. Erickson, E. et al. Comparative performance of PETase as a function of reaction conditions, substrate properties, and product accumulation. *ChemSusChem* **15**, e202101932 (2022).
36. Pfaff, L. et al. Multiple substrate binding mode-guided engineering of a thermophilic PET hydrolase. *ACS Catal.* **12**, 9790–9800 (2022).
37. Heiranian, M., Farimani, A. & Aluru, N. Water desalination with a single-layer MoS2 nanopore. *Nat. Commun.* **6**, 8616 (2015).
38. Gigault, J. et al. Nanoplastics are neither microplastics nor engineered nanoparticles. *Nat. Nanotechnol.* **16**, 501–507 (2021).
39. Johnstone, B. A. et al. Cholesterol-dependent cytolysins: the outstanding questions. *IUBMB Life* **74**, 1169–1179 (2022).
40. 4TSY: crystal structure of FraC with lipids. *NCBI* https://www.ncbi.nlm.nih.gov/Structure/pdb/4TSY
41. 3W9P: crystal structure of monomeric FraC (second crystal form). *NCBI* https://www.ncbi.nlm.nih.gov/Structure/pdb/3W9P
42. Sastry, G. M., Adzhigirey, M., Day, T., Annabhimoju, R. & Sherman, W. Protein and ligand preparation: parameters, protocols, and influence on virtual screening enrichments. *J. Comput. Aided Mol. Des.* **27**, 221–234 (2013).
43. Banks, J. L. et al. Integrated Modeling Program, Applied Chemical Theory (IMPACT). *J. Comput. Chem.* **26**, 1752–1780 (2005).
44. Lecina, D., Gilabert, J. F. & Guallar, V. Adaptive simulations, towards interactive protein–ligand modeling. *Sci. Rep.* **7**, 8466 (2017).
45. Lee, J. et al. CHARMM-GUI input generator for NAMD, GROMACS, AMBER, OpenMM, and CHARMM/OpenMM simulations using the CHARMM36 additive force field. *J. Chem. Theory Comput.* **12**, 405–413 (2016).
46. Bauer, P., Hess, B., & Lindahl, E. GROMACS 2022 Manual. *Zenodo* https://doi.org/10.5281/ZENODO.6103568
47. McGibbon, R. T. et al. MDTraj: a modern open library for the analysis of molecular dynamics trajectories. *Biophys. J.* **109**, 1528–1532 (2015).
48. Michaud-Agrawal, N., Denning, E. J., Woolf, T. B. & Beckstein, O. MDAnalysis: a toolkit for the analysis of molecular dynamics simulations. *J. Comput. Chem.* **32**, 2319–2327 (2011).
49. Abraham, M. J. et al. GROMACS: high performance molecular simulations through multi-level parallelism from laptops to supercomputers. *SoftwareX* **1–2**, 19–25 (2015).
50. Murphy, R. B., Philipp, D. M. & Friesner, R. A. A mixed quantum mechanics/molecular mechanics (QM/MM) method for large-scale modeling of chemistry in protein environments. *J. Comput. Chem.* **21**, 1442–1457 (2000).
51. 5XH3: crystal structure of a novel PET hydrolase R103G/S131A mutant in complex with HEMT from *Ideonella sakaiensis* 201-F6. *NCBI* https://www.ncbi.nlm.nih.gov/Structure/pdb/5XH3
52. Sambrook, J. & Russell, D. W. In vitro mutagenesis using double-stranded DNA templates: selection of mutants with DpnI. *Cold Spring Harb. Protoc.* https://doi.org/10.1101/pdb.prot097766 (2018).
53. Robles-Martín, A. et al. Sub-micro and nano-sized polyethylene terephthalate deconstruction with engineered pore-forming protein nanopores. *Zenodo* https://zenodo.org/deposit/7755566 (2023).

Acknowledgements

This study was conducted under the auspices of the FuturEnzyme Project funded by the European Union's Horizon 2020 Research and Innovation Programme under the auspices of the FuturEnzyme Project (grant agreement no. 101000327) and the PlasticsFatE project (grant agreement no. 95921), and Horizon Europe Research and Innovation Programme under grant agreement no. GA101060625 (Nymphe project). We also acknowledge financial support under grants PID2020-112758RB-I00 (M.F.), PDC2021-121534-I00 (M.F.), TED2021-130544B-I00 (M.F.), PID2019-106370RB-I00 (V.G.) and PID2019-105838RB-C31 (F.J.P.) from the Ministerio de Ciencia e Innovación, Agencia Estatal de Investigación (AEI) (Digital Object Identifier MCIN/AEI/10.13039/501100011033), Fondo Europeo de Desarrollo Regional (ERDF) A way of making Europe and the European Union NextGenerationEU/PRTR, UCM-Banco Santander Grants PR87/19-22556 and PR108/20-26896 and UnaEuropa (Unano) SF2106 (to A.M.P.). S.G.-L. was supported by a Real Colegio Complutense Postdoctoral Fellowship for Distinguished Junior Scholars. S.R. thanks the Spanish Ministry of Science and Innovation for a PhD fellowship (FPU19/00608). D.H.-M. thanks Complutense University of Madrid and Banco Santander for a PhD fellowship (CT82/20/CT83/20). A.R.-M. thanks the Spanish Ministry of Science and Innovation for a PhD fellowship (PRE2020-091825) and the project PID2019-106370RB-I00. We thank M. J. Vicente for the ESI–MS analysis, performed at the Servicio Interdepartamental de Investigación (SIDI) from the Autonomous University of Madrid, Spain.

Author contributions

A.R.-M., R.A.-S., and L.F.-L. contributed equally to this work. V.G., S.G.-L. and M.F. lead this contribution. V.G., A.M.-P. and M.F. wrote the original manuscript, which was further prepared through the contributions of A.R.-M., S.R., S.G.-L., R.P. and M.A.B. All the authors have given approval to the final version of the manuscript. R.A.-S., D.H.-M., A.M.-P. and S.G.-L. contributed to the production, purification and haemolytic and structural characterization of the FraC pore-forming proteins. J.L.G.-A. and F.J.P. contributed to the HPLC analysis. L.F.-L., C.C., D.A. and M.F. performed the ester and

nPET hydrolysis assays and determinations. A.R.-M., S.R. and V.G. contributed to the computational analysis. V.A.-R., R.P. and M.A.B. contributed to the FE-SEM analyses. V.G. originally conceived the computational analysis, which was further experimentally conceived by A.M.-P., S.G.-L. and M.F.

Competing interests
The authors declare no competing interests.

Additional information
Extended data is available for this paper at https://doi.org/10.1038/s41929-023-01048-6.

Supplementary information The online version contains supplementary material available at https://doi.org/10.1038/s41929-023-01048-6.

Correspondence and requests for materials should be addressed to Sara García-Linares, Manuel Ferrer or Víctor Guallar.

Peer review information *Nature Catalysis* thanks Pedro Alexandrino Fernandes, Bian Wu, Ren Wei and the other, anonymous, reviewer(s) for their contribution to the peer review of this work.

Reprints and permissions information is available at www.nature.com/reprints.

Publisher's note Springer Nature remains neutral with regard to jurisdictional claims in published maps and institutional affiliations.

Open Access This article is licensed under a Creative Commons Attribution 4.0 International License, which permits use, sharing, adaptation, distribution and reproduction in any medium or format, as long as you give appropriate credit to the original author(s) and the source, provide a link to the Creative Commons license, and indicate if changes were made. The images or other third party material in this article are included in the article's Creative Commons license, unless indicated otherwise in a credit line to the material. If material is not included in the article's Creative Commons license and your intended use is not permitted by statutory regulation or exceeds the permitted use, you will need to obtain permission directly from the copyright holder. To view a copy of this license, visit http://creativecommons.org/licenses/by/4.0/.

© The Author(s) 2023

https://doi.org/10.1038/s41929-023-01048-6

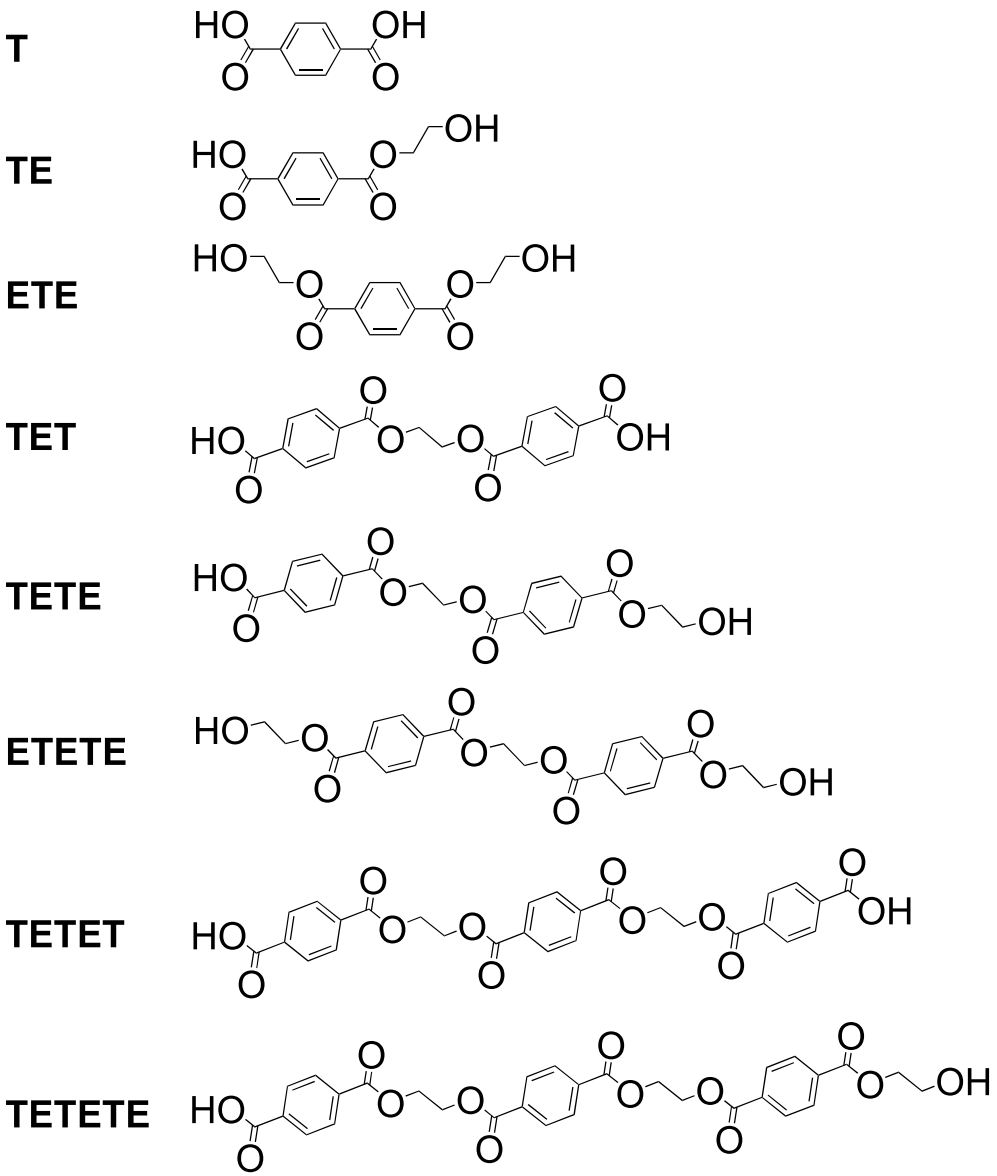

Extended Data Fig. 1 | Chemical structures of the degradation products identified in the present study. The figure was constructed using ChemDraw 18.2. **E** refers to ethylene glycol, **T** refers to terephthalic acid, **TE** refers to MHET, **ETE** refers to BHET, **TETE** refers to $(MHET)_2$ as reported by Joo et al. (2018)[34], and **ETETE** refers to 2-HE$(MHET)_2$ as reported by Joo et al. (2018)[34]. Nomenclature as reported by Schubert et al.[29].

https://doi.org/10.1038/s41929-023-01048-6

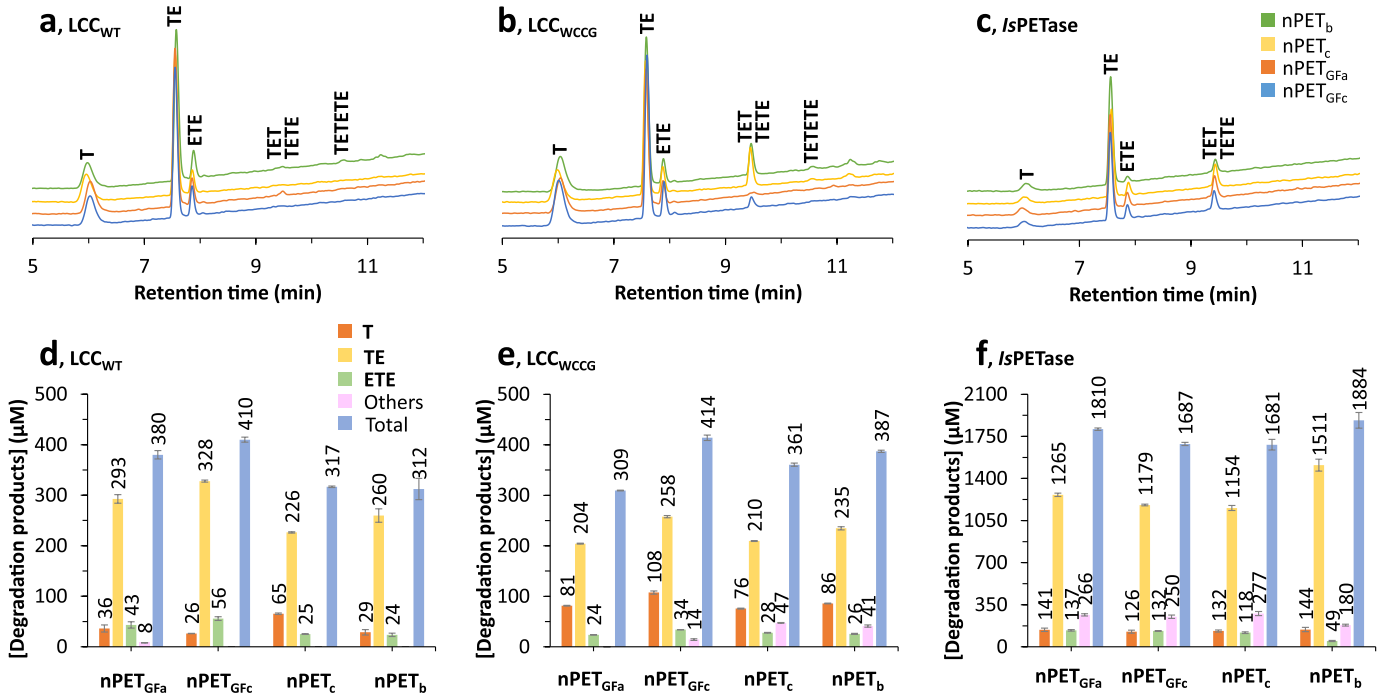

Extended Data Fig. 2 | Degradation profiles of nPET$_{GFa/GFc/b/c}$ treated with *Is*PETase and LCC$_{WT/WCCG}$. a-c HPLC profiles of degradation products released under the experimental conditions: [*Is*PETase, LCC$_{WT/WCCG}$], 1.5 μg ml^{-1}; [nPET$_{GFa/GFc/b/c}$], 1.1 mg ml^{-1}; reaction volume, 1000 μl; T, 40 °C; pH, 7.0 (20 mM HEPES buffer); reaction time, 48 h. The reactions were maintained in 2-ml safe-lock Eppendorf® polypropylene tubes (ref. 0030 120.094) in a thermoshaker (model Thermomixer comfort, Eppendorf AG, Hamburg, Germany) at 1000 rpm. Aliquots of 100 μl were obtained, the reactions were stopped by adding 900 μl dimethyl sulfoxide (from Merck Life Science S.L.U., Madrid, Spain), and the degradation products were immediately analysed by HPLC. Datasets were collected with a Varian Star LC workstation 6.41 (Varian Inc., Palo Alto, California, USA). All reactions and analyses were performed in triplicate (n = 3), with a representative chromatogram per enzyme and nPET particle shown. **d-f** Concentration of degradation products from **T** to **ETETE** corresponding to a-e. Quantification was performed for products with unambiguous identification and for which enough material was recovered for HPLC calibration, namely, from **T** to **ETETE** (Extended Data Fig. 1); purification was performed by semipreparative HPLC, and the molecular weights and structures were determined by mass spectrometry (Supplementary Fig. 15). Values are plotted as the mean of three independent replicates (n = 3) with the reported error ranges and SD calculated using the STDEV.S function in Excel 2019 (calculations and raw data are provided in Source Data). The figure was constructed using Excel 2019. Raw data are shown in Supplementary Data 9.

https://doi.org/10.1038/s41929-023-01048-6

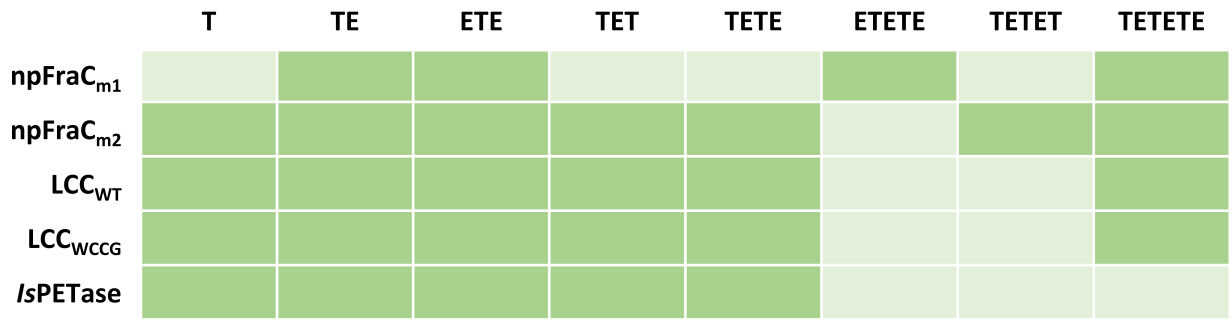

Extended Data Fig. 3 | Schematic of the degradation product profiles. The degradation products identified after nPET hydrolysis by npFraC$_{m1}$, npFraC$_{m2}$, LCC$_{WT}$, LCC$_{WCCG}$ and *Is*PETase are shown.

https://doi.org/10.1038/s41929-023-01048-6

Extended Data Table 1 | Ester-hydrolysing activity of npFraC$_{m1}$ and npFraC$_{m2}$

Substrate	npFraC$_{m1}$	npFraC$_{m2}$
	Specific activity (U mg^{-1})	
p-NPB[1]	17.80±1.50	337.1±33.9
p-NPP[1]	14.50±1.00	277.8±28.6
p-NPA[1]	6.70±0.30	142.6±9.0
Glyceryl tripropionate[2]	39.89±3.70	18.27±1.09
Vinyl acetate[2]	31.40±0.11	27.24±2.12
Phenyl acetate[2]	70.94±3.97	3.93±0.54
TE[2,3]	0.09±0.01	2.44±0.37
ETE[2]	0.15±0.02	1.03±0.10

[1]Reaction conditions for p-NP esters: [npFraC$_{m1/m2}$], 18.3 µg ml^{-1}; [p-NP ester], 7 mM; reaction volume, 200 µl; T, 40 °C; pH, 7.0 (4-(2-hydroxyethyl)piperazine-1-ethanesulfonic acid (HEPES) buffer, 40 mM); assay format, 96-well plates (ref. 655801, Greiner Bio-One GmbH, Kremsmünster, Austria); assay wavelength, 348 nm; ε = 4147 M^{-1} cm^{-1}. [2]Reaction conditions for substrates other than p-NP esters: [npFraC$_{m1}$ or npFraC$_{m2}$], 18.3 µg ml^{-1}; [glyceryl tripropionate, phenyl acetate, vinyl acetate, **TE**, or **ETE**], 20 mM; reaction volume, 44 µl; T, 40 °C; pH, 8.0 (4-(2-hydroxyethyl)-1-piperazinepropanesulfonic acid, EPPS, buffer, 5 mM); format: 384-well plates (ref. 781162, Greiner Bio-One GmbH); assay wavelength: 550 nm; ε = 8450 M^{-1} cm^{-1}. Datasets were collected with a Synergy HT Multi-Mode Microplate reader (BioTek Instruments, Winooski, VT, USA) with Gen5 2.00 software, with values obtained from the best linear fit using SigmaPlot 14.5. [3]No conversion was detected using the colorimetric assay detailed in[2] because of minimal conversion, which is why specific activity was determined after examining the reaction product by HPLC. Abbreviations are listed as follows: p-NPA, p-nitrophenyl acetate; p-NPP, p-nitrophenyl propionate; p-NPB, p-nitrophenyl butyrate. Values are plotted as the mean of three independent replicates (*n* = 3) with the reported error ranges and standard deviations (SD) calculated using the STDEV.S function in Excel 2019 (calculations and raw data are provided in Source Data). Raw data are shown in Supplementary Data 3. **TE** and **ETE** are highlighted in bold as these are not standard nomenclatures of chemical products but abbreviations, according to Schubert et al.[29]

https://doi.org/10.1038/s41929-023-01048-6

Extended Data Table 2 | Physical-chemical characteristics of the PET materials and nPET particles

PET material	T_G[2], °C	Crystallinity[2,3], %	T_M[2], °C	T_C[2], °C	H_c[2], J/g	∅[4], nm
PET_c[1]	74.7	34.5	234.8 (T_{m1}), 248.1 (T_{m2})	-	-	–
PET_b[1]	75.1	24.3	248.0	192.8	37.9	–
PET_{GFa}[1]	72.0	1.3	246.7	200.6	32.8	–
PET_{GFc}[1]	73.7	31.3	251.9	202.1	44.1	–
$nPET_c$	75.7	7.0	247.2	193.2	37.8	53.1±0.1 (21.0-91.3)
$nPET_b$	73.3	5.0	248.6	213.6	38.1	108.0±0.1 (58.5-255)
$nPET_{GFa}$	73.7	14.0	245.9	199.6	41.5	80.47±0.1 (43.8-190)
$nPET_{GFc}$	75.5	14.8	250.5	215.1	49.7	65.87±0.1 (37.8-142)

[1]Thickness of raw PET material, as measured with a stainless steel Mitutoyo dial calliper (ref. 99MAC005B; MSC, Wednesbury, United Kingdom): PET_c, length (2.31±0.24 mm), width (2.13±0.12 mm) and height (2.87±0.17 mm); PET_b, 0.21±0.02 mm; PET_{GFa}, 0.25 mm; PET_{GFc}, 0.25 mm. [2]T_G, T_M, T_C, crystallinity (%), and ΔH_c, determined using dry nPET or PET material by DSC (Supplementary Fig. 13). [3]Crystallinity (%) was calculated from the DSC datasets considering ΔH^0_m (T_m) = 140 J/g, as described in the Supplementary Methods. [4]∅, Diameter of the sub-micro and nanoparticles, determined using nPET suspensions by DLS. Data are given as the mean of three independent replicates (n = 3), with values in the range ±0.5, if otherwise not indicated.

nature portfolio

Corresponding author(s): Sara García-Linares, Manuel Ferrer, Víctor Guallar

Last updated by author(s): Aug 25, 2023

Reporting Summary

Nature Portfolio wishes to improve the reproducibility of the work that we publish. This form provides structure for consistency and transparency in reporting. For further information on Nature Portfolio policies, see our Editorial Policies and the Editorial Policy Checklist.

Statistics

For all statistical analyses, confirm that the following items are present in the figure legend, table legend, main text, or Methods section.

n/a	Confirmed
☐	☒ The exact sample size (*n*) for each experimental group/condition, given as a discrete number and unit of measurement
☐	☒ A statement on whether measurements were taken from distinct samples or whether the same sample was measured repeatedly
☒	☐ The statistical test(s) used AND whether they are one- or two-sided *Only common tests should be described solely by name; describe more complex techniques in the Methods section.*
☒	☐ A description of all covariates tested
☒	☐ A description of any assumptions or corrections, such as tests of normality and adjustment for multiple comparisons
☐	☒ A full description of the statistical parameters including central tendency (e.g. means) or other basic estimates (e.g. regression coefficient) AND variation (e.g. standard deviation) or associated estimates of uncertainty (e.g. confidence intervals)
☒	☐ For null hypothesis testing, the test statistic (e.g. *F*, *t*, *r*) with confidence intervals, effect sizes, degrees of freedom and *P* value noted *Give P values as exact values whenever suitable.*
☒	☐ For Bayesian analysis, information on the choice of priors and Markov chain Monte Carlo settings
☒	☐ For hierarchical and complex designs, identification of the appropriate level for tests and full reporting of outcomes
☒	☐ Estimates of effect sizes (e.g. Cohen's *d*, Pearson's *r*), indicating how they were calculated

Our web collection on statistics for biologists contains articles on many of the points above.

Software and code

Policy information about availability of computer code

Data collection

- Computational data has been collected with Protein Energy Landscape Exploration (PELE) (version rev12360).
- Molecular dynamics simulations have been collected with GROMACS (version 5.1.2) and OPENMM (version 7.3)
- Datasets for ester hydrolysis have been collected from a Synergy HT Multi-Mode Microplate Reader with Gen5 2.00 software (Biotek Instruments, Winooski, VT, USA).
- Dynamic light scattering (DLS) datasets have been collected with a Malvern Instrument (MALVERN ZETASIER NANO S ZEN 1600, IESMAT, Madrid, Spain) with a Dispersion Technology software 4.20 (Malvern Instrument Ltd.).
- Field emission scanning electron microscopy (FE-SEM) was performed with a FEI Nova NanoSEM 230 microscope and the particle size was measured using ImageJ (NIH) software.
- High-Performance liquid chromatography (HPLC) datasets have been collected with a Varian Star LC workstation 6.41 (Varian, Inc., Walnut Creek, CA, USA).
- Electron microscopy datasets have been collected with JEOL JEM1400 transmission electron microscope and processed using a DigitalMicrograph software (Gatan Inc.).
- Far-UV circular dichroism (CD) spectra were recorded on a Jasco 715 spectropolarimeter (Jasco Inc., Tokyo, Japan) and processed with a Spectra Manager software (Jasco Inc., Tokyo, Japan).
- Fluorescence emission spectra have been recorded on an SLM Aminco 8000 spectrofluorimeter and processed with a SLM software (Aminco, Maryland, USA).

Data analysis

- Computational data analysis was performed with Protein Energy Landscape Exploration (PELE) (version rev12360).
- Analysis of molecular dynamics simulations was performed with GROMACS (version 5.1.2) and OPENMM (version 7.3)
- Analysis of ester hydrolysis hwas performed with Gen5 2.00 software (Biotek Instruments, Winooski, VT, USA), Excel 2019 and Sigma Plot version 14.5).
- Dynamic light scattering (DLS) datasets have been analysed with a Dispersion Technology software 4.20 (Malvern Instrument Ltd.).
- The particle size measured by field emission scanning electron microscopy, was analysed using ImageJ (NIH) software.
- Electron microscopy datasets have been processed using a DigitalMicrograph software (Gatan Inc.).

- Far-UV circular dichroism (CD) spectra data was processed with a Spectra Manager software (Jasco Inc., Tokyo, Japan).
- Fluorescence emission spectra data have been processed with a SLM software (Aminco, Maryland, USA).

For manuscripts utilizing custom algorithms or software that are central to the research but not yet described in published literature, software must be made available to editors and reviewers. We strongly encourage code deposition in a community repository (e.g. GitHub). See the Nature Portfolio guidelines for submitting code & software for further information.

Data

Policy information about availability of data

All manuscripts must include a data availability statement. This statement should provide the following information, where applicable:

- Accession codes, unique identifiers, or web links for publicly available datasets
- A description of any restrictions on data availability
- For clinical datasets or third party data, please ensure that the statement adheres to our policy

Raw values for all other data in figures and analyses are available without any restriction in the Supplementary Data.

Field-specific reporting

Please select the one below that is the best fit for your research. If you are not sure, read the appropriate sections before making your selection.

☒ Life sciences ☐ Behavioural & social sciences ☐ Ecological, evolutionary & environmental sciences

For a reference copy of the document with all sections, see nature.com/documents/nr-reporting-summary-flat.pdf

Life sciences study design

All studies must disclose on these points even when the disclosure is negative.

Sample size	No sample-size calculation was performed as the study related to the analysis of proteins and proteins nanopores (native or containing specific mutations).
Data exclusions	No data were excluded.
Replication	For Table 1, Figure 5c, Figure 5d, Figure 6, Figure 7, Extended Data Table 1, Supplementary Fig. 10, Supplementary Fig. 11, Supplementary Fig. 14, Supplementary Fig. 16, Supplementary Fig. 17, values are plotted as the mean of three independent replicates (n = 3) with the reported error ranges and standard deviations (SD) calculated using the STDEV.S function in Excel 2019. For Figure 5a and Figure 5b, values are plotted as the mean of three independent replicates (n = 3) with the reported error ranges and SD calculated using Dispersion Technology software 4.20 (Malvern Instrument Ltd.). For Supplementary Figures 3, 4 and 6, the number of samples for the different molecular dynamics simulations was 4 (n = 4, independent replicates). For Supplementary Figure 5, the number of samples for the different molecular dynamics simulations was 1 (n = 1). For Supplementary Figure 8c, each value is the average ± standard error of the mean from three different independent experiments (n = 3). For Supplementary Figure 8d, each value is the average ± standard error of the mean from two different independent experiments (n = 2). For Supplementary Fig. 12, thermal denaturation monitored by circular dichroism at 220 nm was performed in independent triplicates (n = 3). For Supplementary Fig. 18, the FE-SEM the size distribution was based on the measurements of at least 200 individual random particles.
Randomization	This is not relevant to the study, as the study related to the analysis of thre soluble proteins and three protein nanopores (one native, and two containing specific mutations).
Blinding	Blinding was not relevant as the study related to the characterization of two soluble proteins and two proteins nanopores (native or containing specific mutations). Their identities and confirmation of specific mutations introduced were firstly confirmed by DNA sequencing. Each protein material was produced and characterized.

Reporting for specific materials, systems and methods

We require information from authors about some types of materials, experimental systems and methods used in many studies. Here, indicate whether each material, system or method listed is relevant to your study. If you are not sure if a list item applies to your research, read the appropriate section before selecting a response.

Materials & experimental systems

n/a	Involved in the study
☒	☐ Antibodies
☒	☐ Eukaryotic cell lines
☒	☐ Palaeontology and archaeology
☒	☐ Animals and other organisms
☒	☐ Human research participants
☒	☐ Clinical data
☒	☐ Dual use research of concern

Methods

n/a	Involved in the study
☒	☐ ChIP-seq
☒	☐ Flow cytometry
☒	☐ MRI-based neuroimaging